iScience

CellPress OPEN ACCESS

Article

INPP5D modulates TREM2 loss-of-function phenotypes in a β-amyloidosis mouse model

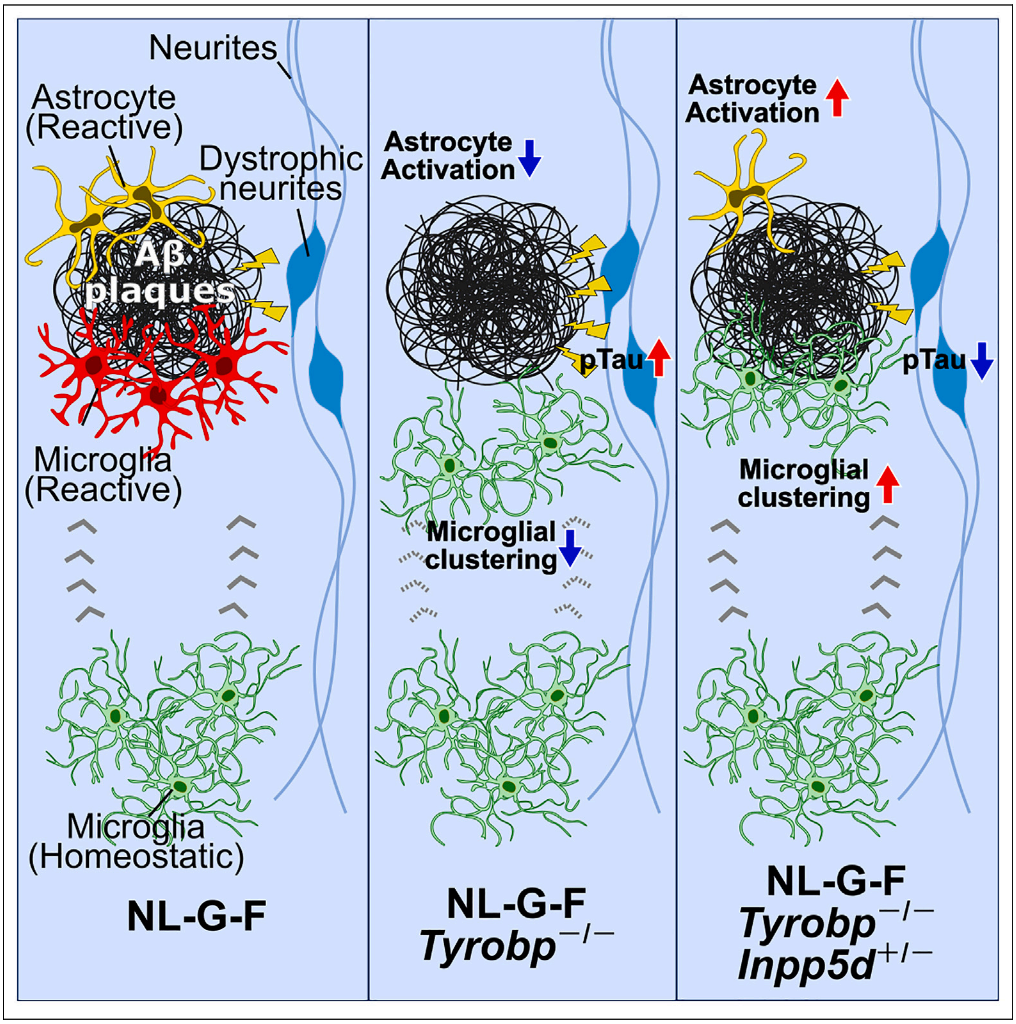

Akihiro Iguchi, Sho Takatori, Shingo Kimura, ..., Toshiyuki Takai, Takehiko Sasaki, Taisuke Tomita

taisuke@mol.f.u-tokyo.ac.jp

Highlights

Inpp5d haplodeficiency rescues microglial loss around Aβ plaques in Tyrobp KO mice

Restored microglia affect plaque compaction, astrogliosis, and p-tau deposition

TREM2/TYROBP and INPP5D exert opposing effects on a common PI3K signaling pathway

Iguchi et al., iScience *26*, 106375
April 21, 2023
https://doi.org/10.1016/j.isci.2023.106375

iScience

CellPress
OPEN ACCESS

Article

INPP5D modulates TREM2 loss-of-function phenotypes in a β-amyloidosis mouse model

Akihiro Iguchi,[1,8] Sho Takatori,[1,8] Shingo Kimura,[1] Hiroki Muneto,[1] Kai Wang,[1] Hayato Etani,[1] Genta Ito,[2] Haruaki Sato,[1] Yukiko Hori,[1] Junko Sasaki,[3] Takashi Saito,[4,5] Takaomi C. Saido,[4] Tsuneya Ikezu,[6] Toshiyuki Takai,[7] Takehiko Sasaki,[3] and Taisuke Tomita[1,9,*]

SUMMARY

The genetic associations of TREM2 loss-of-function variants with Alzheimer disease (AD) indicate the protective roles of microglia in AD pathogenesis. Functional deficiencies of TREM2 disrupt microglial clustering around amyloid β (Aβ) plaques, impair their transcriptional response to Aβ, and worsen neuritic dystrophy. However, the molecular mechanism underlying these phenotypes remains unclear. In this study, we investigated the pathological role of another AD risk gene, *INPP5D*, encoding a phosphoinositide PI(3,4,5)P_3 phosphatase expressed in microglia. In a *Tyrobp*-deficient TREM2 loss-of-function mouse model, *Inpp5d* haplodeficiency restored the association of microglia with Aβ plaques, partially restored plaque compaction, and astrogliosis, and reduced phosphorylated tau$^+$ dystrophic neurites. Mechanistic analyses suggest that TREM2/TYROBP and INPP5D exert opposing effects on PI(3,4,5)P_3 signaling pathways as well as on phosphoproteins involved in the actin assembly. Our results suggest that INPP5D acts downstream of TREM2/TYROBP to regulate the microglial barrier against Aβ toxicity, thereby modulates Aβ-dependent pathological conversion of tau.

INTRODUCTION

Alzheimer disease (AD) is pathologically characterized by the extracellular deposition of amyloid β (Aβ) fibrils in the brain parenchyma, the intraneuronal aggregation of tau proteins, and neuronal cell loss. The Aβ deposition drives the pathogenesis of AD, while tau aggregation is directly linked to neuronal dysfunction and ultimately cell death. Furthermore, recent whole-exome sequencing and genome-wide association studies have suggested that microglia also contribute to the pathogenesis of AD.[1–3]

A rare variant of triggering receptor expressed on myeloid cells 2 (*TREM2*) (p.R47H) is associated with the second-highest odds ratio for late-onset AD after *APOE* ε4.[4,5] *TREM2* encodes a microglia-specific transmembrane receptor, which recognizes various extracellular ligands (e.g. lipids, Aβ, and lipoproteins) and transmits signals via its binding partner, TYRO protein tyrosine kinase-binding protein (TYROBP), to downstream targets, including Syk, phosphoinositide 3-kinases (PI3Ks), and mitogen-activated protein kinases (MAPKs).[6–9] AD-associated TREM2 variants disrupt TREM2-ligand interaction,[10–15] suggesting a loss-of-function mechanism underlying the AD pathogenesis. Loss or disease-associated mutations of TREM2 affect microglial clustering around amyloid plaques in mouse models of Aβ pathology as well as in human, and exacerbate neuritic dystrophy around plaques.[11,16–20] Importantly, dystrophic neurites are regarded as the place where tau is phosphorylated and aggregated,[21] and *Trem2* deficiency accelerates it only when Aβ pathology is present.[22,23] These suggest a crucial protective role of microglia and TREM2 in Aβ-driven spreading of tau pathology.[24] Moreover, TREM2 sustains microglial proliferation/survival,[11] maintains energy metabolism of microglia,[25,26] permits conversion of homeostatic microglia into disease-associated microglia (DAM)[27] or neurodegenerative microglia,[28] and regulates cerebral glucose uptake by microglia.[29–31] These beneficial roles of TREM2 may offer a therapeutic opportunity in AD. Indeed, TREM2 agonistic antibodies enhance microglial responses to Aβ, promote microglial proliferation, and reduce Aβ burden and its neurotoxic effects[32–36] and are starting to enter clinical trials to test their therapeutic potential.

Considering the important roles of TREM2, it is reasonable to assume that other AD risk genes also converge on the same pathway. Among them, we focused on inositol polyphosphate-5-phosphatase D

[1]Laboratory of Neuropathology and Neuroscience, Graduate School of Pharmaceutical Sciences, The University of Tokyo, 7-3-1 Hongo, Bunkyo-ku, Tokyo 113-0033, Japan

[2]Department of Biomolecular Chemistry, Faculty of Pharma-Science, Teikyo University, 2-11-1 Kaga, Itabashi-ku, Tokyo 173-8605, Japan

[3]Department of Lipid Biology, Medical Research Institute, Tokyo Medical and Dental University, 1-5-45 Yushima, Bunkyo-ku, Tokyo 113-8510, Japan

[4]Laboratory for Proteolytic Neuroscience, RIKEN Center for Brain Science, 2-1 Hirosawa, Wako, Saitama 351-0198, Japan

[5]Department of Neurocognitive Science, Institute of Brain Science, Nagoya City University Graduate School of Medical Science, 1 Kawasumi, Mizuho-cho, Mizuho-ku, Nagoya, Aichi 467-8601, Japan

[6]Department of Neuroscience, Mayo Clinic Florida, Jacksonville, FL 32224, USA

[7]Department of Experimental Immunology, Institute of Development, Aging and Cancer, Tohoku University, 4-1 Seiryo, Sendai 980-8575, Japan

[8]These authors contributed equally

[9]Lead contact

*Correspondence: taisuke@mol.f.u-tokyo.ac.jp

https://doi.org/10.1016/j.isci.2023.106375

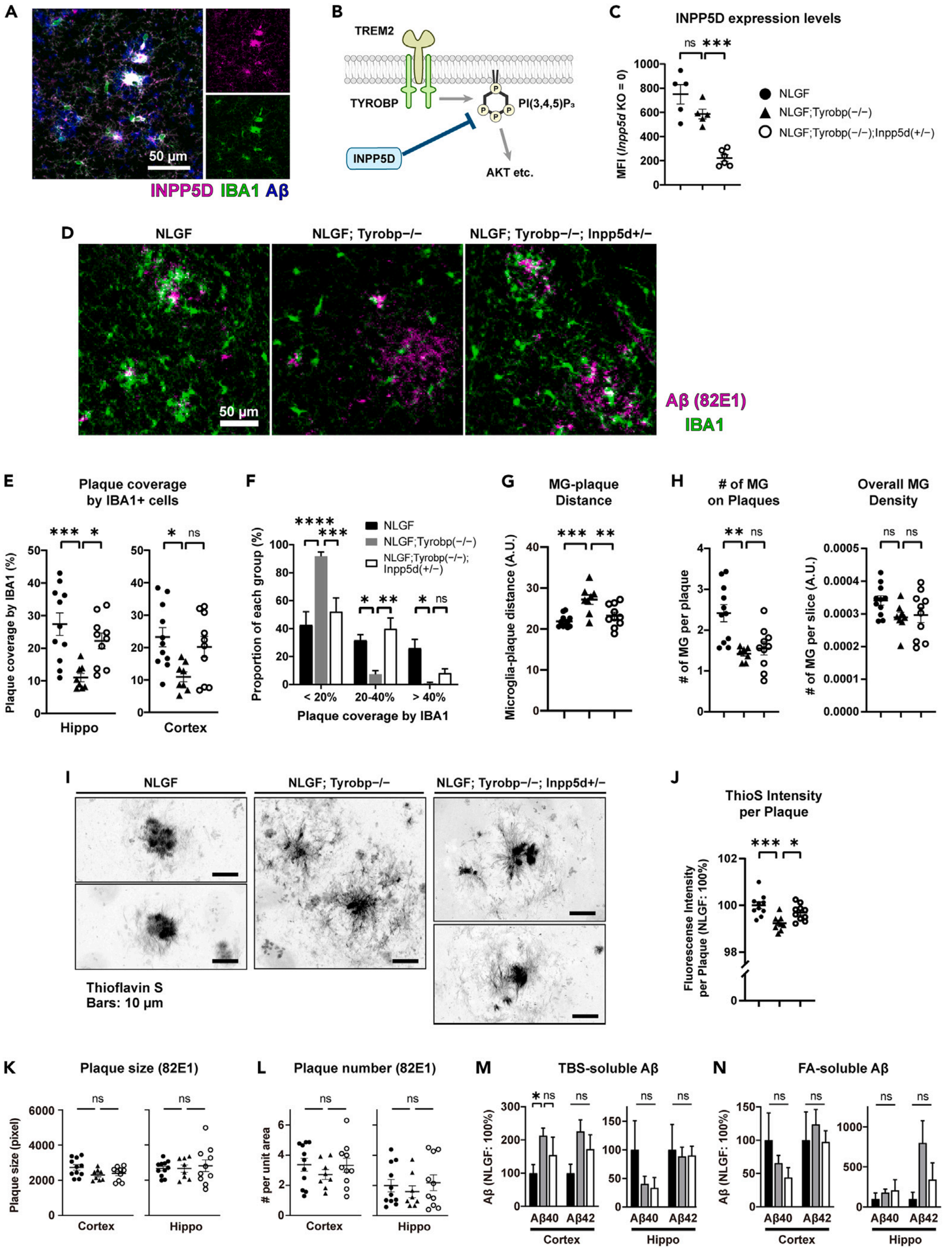

Figure 1. Inpp5d haplodeficiency restored microglial clustering around amyloid plaques in Tyrobp-deficient NLGF mice

(A) Immunohistochemistry for INPP5D (*magenta*), IBA1 (*green*), and A$\beta_{1\text{-x}}$ (*blue*) in the brain cortical area of *NLGF* mouse. Scale bar: 50 µm.

(B) Schematic showing inhibitory role of INPP5D on the TREM2/TYROBP-mediated PI(3,4,5)P_3 signaling pathway.

(C) Flow cytometric quantification of INPP5D in isolated microglia from 5-month-old mice. Mean fluorescence intensity (MFI) of each genotype was shown after subtracting the value for *Inpp5d*$^{-/-}$;*NLGF* microglia (N = 2) as a background.

(D) Immunohistochemistry for IBA1 (*green*) and A$\beta_{1\text{-x}}$ (*magenta*) in the hippocampal region of the indicated genotypes. Scale bar: 50 µm.

(E) Quantification of the plaque coverage by IBA1-positive cells (%) in the hippocampus and cortex.

(F) Frequency distribution of the plaque coverage by IBA1-positive cells, classified into dense (>40%), intermediate (20%–40%) and sparse (<20%).

Figure 1. *Continued*

(G) Quantification of the mean distance of PU.1-positive myeloid cells from the center of the plaque in the hippocampus.

(H) The number of plaque-associated myeloid cells per plaque (*right*) and the overall density of myeloid cells (*left*) in the hippocampus were assessed by PU.1 staining (N = 8–11).

(I) Representative super-resolution images of Thioflavin S-labeled Aβ plaques of the indicated mice. Note that the brightness/contrast of images was differently adjusted for each image to highlight the morphological differences between groups. Scale bar: 10 μm.

(J) The mean fluorescence intensity of thioflavin labeling on plaques was determined and shown by normalizing to the average of *NLGF* group as 100% (N = 9–10).

(K and L) The size (*K*) and number (*L*) of plaques in the brain slices from the indicated mice were determined by anti-$A\beta_{1\text{-}x}$ antibody (82E1) staining for the cortex and hippocampus (Hippo) (N = 8–11).

(M and N) Abundance of Aβ40 and Aβ42 in TBS-soluble (*M*) and FA-soluble (*N*) fractions was determined from the cortex and hippocampus of the indicated mice by ELISA. Data were represented by normalizing to *NLGF* mice as 100% (N = 3–11). Each point represents an individual mouse. Bars represent the mean ± SEM of all analyzed animals in each genotype. Nine-month-old male mice were analyzed except for *C*. One-way ANOVA was used except for *F* using two-way ANOVA, followed by Tukey's multiple comparisons. ns: not significant ($p > 0.05$), *$p < 0.05$, **$p < 0.01$, ***$p < 0.001$, ****$p < 0.0001$. See also Figures S1–S3.

(*INPP5D*), a gene specifically expressed in microglia in the brain.[2] INPP5D hydrolyzes phosphatidylinositol-(3,4,5)-trisphosphate [$PI(3,4,5)P_3$] at its 5′-position and negatively regulates the function of this lipid second messenger.[37] Since $PI(3,4,5)P_3$ activates many signaling molecules such as AKT serine/threonine kinase (AKT), INPP5D regulates a broad range of cellular events, including inflammation, cell proliferation, and cell motility.[38] An AD risk variant of *INPP5D* (rs35349669) is associated with increased expression of INPP5D protein.[39] In particular, this intronic polymorphism is thought to upregulate a specific truncated isoform of unknown function by promoting its internal transcription initiation.[2] Intriguingly, INPP5D inhibits TREM2 signaling during osteoclastogenesis.[40] However, the role of INPP5D in AD pathogenesis has not been investigated.

In this study, we aimed to clarify the pathological role of INPP5D in mutant *App* knockin AD model mice (*$App^{NL\text{-}G\text{-}F/NL\text{-}G\text{-}F}$*; hereafter *NLGF*).[41] *Inpp5d*-haplodeficient *NLGF* mice showed no effects on Aβ burden or plaque-associated changes of microglia, astrocytes, or neurites. In *Tyrobp*-deficient *NLGF* mice, however, *Inpp5d* reduction ameliorated the impaired microglial clustering around plaques, which was associated with plaque compaction, the reappearance of reactive astrocytes, and the reduction of phosphorylated tau in nearby neurites. Bulk RNA sequencing (RNA-seq) analysis of isolated microglia and immunohistochemical profiling showed that *Inpp5d* haplodeficiency had a minor rescue effect on DAM signature gene expression in *Tyrobp*-deficient microglia. Instead, an improvement in microglial adhesion to amyloid plaques or an increase in $PI(3,4,5)P_3$ levels was suggested. These data suggest that *Inpp5d* haplodeficiency ameliorates several defects in *Tyrobp*-deficient mouse microglia, thereby affecting p-tau deposition.

RESULTS

Inpp5d haplodeficiency ameliorates the pathological changes in Tyrobp-deficient NLGF mice

In *NLGF* mice, brain expression of INPP5D was restricted in parenchymal microglia and particularly high in plaque-associated microglia (Figure 1A), similar to a previous report.[42] To test the pathological role of INPP5D, we investigated the effect of *Inpp5d* haplodeficiency in *NLGF* mice, as homozygous but not heterozygous *Inpp5d* knockout mice develop lethal pulmonary inflammation.[43] However, *$Inpp5d^{+/-}$;NLGF* mice did not show any detectable difference in Aβ deposition, microglial accumulation around amyloid plaques, astrocyte activation, or neurite dystrophy compared with *NLGF* mice (Figures S1 and S2).

TREM2/TYROBP exerts its neuroprotective function possibly via their downstream molecules including PI3K.[25,44] Consistently, gene ontology (GO) term enrichment analysis of publicly available RNA-seq data[20] showed enrichment for the term related to PI3K pathway as being downregulated by *Trem2* deficiency (Figure S3A). Considering that INPP5D inhibits PI3K functions and has an antagonistic role against TREM2 signaling,[40] we hypothesized that INPP5D negatively regulates TREM2/TYROBP functions in the brain (Figure 1B).

To investigate their genetic interaction *in vivo*, we asked whether *Inpp5d* haplodeficiency could modulate phenotypes of *$Tyrobp^{-/-}$;NLGF* mice. Reduced expression of INPP5D was first confirmed in isolated microglia from *Inpp5d*$^{+/-}$;*Tyrobp*$^{-/-}$;*NLGF* mice by flow cytometry (Figure 1C) as well as by immunoblotting of whole brain lysates (Figures S3B and S3C). We then performed immunohistochemistry of the brains for Aβ and IBA1 (a myeloid cell marker) to analyze microglial association with plaques (Figure 1D). At 9 months of age, *Tyrobp*$^{-/-}$;*NLGF* mice showed reduced microglial coverage of plaques versus *NLGF* mice, as assessed by the overlap of Aβ and IBA1 staining (Figures 1E and S3D). Specifically, the proportions of plaques showing high and intermediate (>20%) microglial coverage were decreased, whereas that of low (<20%) coverage was increased (Figure 1F). Interestingly, additional haplodeficiency of *Inpp5d* almost normalized these defects (Figures 1E, 1F, and S3D). P2RY12-positive (brain resident) microglia were comparable between *Inpp5d*$^{+/-}$;*Tyrobp*$^{-/-}$;*NLGF* and *NLGF* mice (Figure S3E), suggesting that the repopulated cells are of brain origin. Immunolabeling of PU.1, which visualizes microglial nuclei,[45] revealed that the distance between individual plaques and surrounding microglia was affected in *Tyrobp*$^{-/-}$;*NLGF* mice, but it was also restored in *Inpp5d*$^{+/-}$;*Tyrobp*$^{-/-}$;*NLGF* mice (Figures 1G and S3F). For the number of plaque-associated microglia, *Tyrobp*$^{-/-}$;*NLGF* mice showed a significant reduction compared with *NLGF* mice, without affecting the overall density of microglia in brain sections (Figure 1H). Interestingly, however, *Inpp5d* haplodeficiency did not restore the number of plaque-associated microglia in *Tyrobp*$^{-/-}$;*NLGF* mice. Taken together, these suggest that *Inpp5d* deficiency restores the microglial association with plaques, rather than promoting their proliferation/survival.

Microglia form a physical barrier around Aβ deposits and promote the compaction of Aβ into inert, dense core plaques. Impaired microglia-plaque association in *Trem2*- or *Tyrobp*-deficient mice leads to plaque remodeling into a filamentous shape.[17,18,20,46] We therefore stained amyloid plaques with Thioflavin S, which only detects inert plaques, and examined their morphology using super-resolution microscopy (Figure 1I). In contrast to the compact morphology of the plaques in *NLGF* mice, plaques in *Tyrobp*-deficient mice were often devoid of such a dense core, and instead were composed of reticular fibrils radiating from the vacant center. Notably, the plaques of *Inpp5d*$^{+/-}$;*Tyrobp*$^{-/-}$;*NLGF* mice demonstrated intermediate morphological characteristics between those of *NLGF* and *Tyrobp*$^{-/-}$;*NLGF* mice; the plaques had a dense central core and were surrounded by fibrillar Aβ deposits. Quantification of the plaque-associated thioflavin fluorescence showed a significant reduction of the staining in *Tyrobp*-deficient *NLGF* mice, and the reduction was corrected by additional *Inpp5d* haplodeficiency (Figure 1J). Next, we asked whether *Inpp5d* haplodeficiency affects Aβ burden by anti-Aβ antibody (82E1) staining, which visualizes filamentous Aβ deposition. There was no detectable difference in the size or the number of plaques among *NLGF*, *Tyrobp*$^{-/-}$;*NLGF*, and *Inpp5d*$^{+/-}$;*Tyrobp*$^{-/-}$;*NLGF* mice (Figures 1K, 1L, and S3G). In addition, the amounts of Aβ40 and Aβ42 in the Tris-buffered saline-soluble and the formic acid-soluble fractions of brains were almost indifferent among all the genotypes (Figures 1M and 1N). In summary, *Inpp5d* reduction restores plaque morphology in *Tyrobp*-deficient *NLGF* mice without affecting Aβ burden by facilitating the microglial clustering around plaques.

Reactive microglia trigger astrocyte activation that is also implicated in the amyloid pathology in mice and humans.[47,48] Astrocytes in *NLGF* mice were activated around plaques, as indicated by glial fibrillary acidic protein (GFAP) positivity (Figure 2A), which is absent in the cortex of wild-type mice.[49,50] The immunoreactivity was reduced in *Tyrobp*$^{-/-}$;*NLGF* mice (Figure S4), similar to previous findings that *Trem2* deficiency or microglial depletion reduces astrocyte activation.[17,20,51,52] Interestingly, *Inpp5d* haplodeficiency restored the GFAP expression in *Tyrobp*$^{-/-}$;*NLGF* mice (Figures 2A and 2B). These results suggest that astrocyte activation depends on the physical association of microglia with amyloid plaques, which is restored by haplodeficiency of *Inpp5d*.

Apolipoprotein E (ApoE) is a unique factor that facilitates both plaque-associated microgliosis and plaque compaction.[53] While ApoE is predominantly expressed by astrocytes, it is upregulated by plaque-associated microglia. In addition, recent reports in β-amyloidosis mice showed that *Trem2* deficiency affects the abundance of plaque-associated ApoE.[20,54] We therefore asked whether *Inpp5d* deficiency alters ApoE deposition around plaques and whether such alteration correlates with observed changes in microgliosis, astrogliosis, and plaque morphology. In *NLGF* mice, ApoE immunoreactivity was prominent around amyloid plaques (Figure 3A), but the labeling was unchanged in *Tyrobp*$^{-/-}$;*NLGF* mice unlike *Trem2*-deficient mice (Figure 3B). In contrast, the ApoE deposition was significantly upregulated in *Inpp5d*$^{+/-}$;*Tyrobp*$^{-/-}$;*NLGF* mice, revealing an unexpected role of INPP5D in the ApoE regulation. However, no obvious change of plaque-associated ApoE in *Tyrobp*$^{-/-}$;*NLGF* mice suggests that ApoE is not a sole factor that can explain the phenotypes observed in our models.

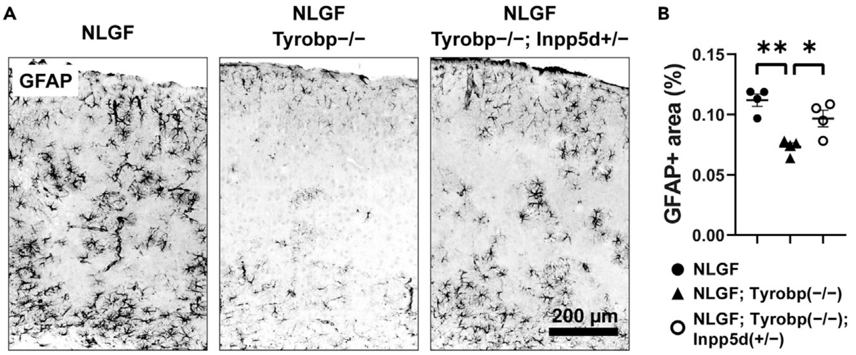

Figure 2. Inpp5d haplodeficiency restored astrocytic activation in Tyrobp-deficient NLGF mice

(A) Representative images of GFAP staining around the somatosensory cortex. Scale bar: 200 μm.

(B) Quantification of the GFAP-positive area (%) per unit area of the cortex (N = 4). Each point represents an individual mouse. Bars represent the mean ± SEM of all analyzed animals in each genotype. Nine-month-old male mice were analyzed. One-way ANOVA followed by Tukey's multiple comparisons. ns: not significant ($p > 0.05$), $^{*}p < 0.05$, $^{**}p < 0.01$. See also Figure S4.

Dystrophic neurite is an axonal swelling surrounding plaques, which reflects neuronal damage by Aβ. Because microglia restrain the dystrophic neurite formation by encapsulating plaques,[18,55] we asked the effect of *Inpp5d* haplodeficiency on this phenotype. We first examined beta-site APP cleaving enzyme 1 (BACE1), a known marker of dystrophic neurites.[56] *Tyrobp*$^{-/-}$*;NLGF* mice had a larger BACE1-immunoreactive area compared with *NLGF* mice. However, additional *Inpp5d* haplodeficiency did not affect the BACE1 deposition (Figure 4A). Considering that the molecular composition of dystrophic neurite is changed in disease progression,[57] we also analyzed other markers, namely, LAMP1,[55] ubiquitin,[58] and phosphorylated tau (p-tau; pS202/pT205).[17,18] Similar to BACE1, the levels of these proteins around plaques were increased in *Tyrobp*$^{-/-}$*;NLGF* mice compared with *NLGF* mice (Figures 4B–4D). Interestingly, p-tau immunoreactivity was specifically attenuated around plaques of *Inpp5d*$^{+/-}$*;Tyrobp*$^{-/-}$*;NLGF* mice, whereas that of neither LAMP1 nor ubiquitin was altered compared with *Tyrobp*-deficient mice (Figure 4D). To ask why this effect is specific to p-tau, we compared the accumulation of p-tau and BACE1 in disease progression (Figure 5A). As expected, overall levels of both markers increased concomitantly with amyloid deposition (Figures 5B and 5C). However, the mean intensity of BACE1 per plaque area was already high as early as 4 months of age and remained constant among all ages, while that of p-tau showed a unique age-dependent increase (Figure 5D). Furthermore, p-tau and BACE1 were found in juxtaposed but different dystrophic neurites (Figure 5A), as previously described.[22] These suggest that p-tau accumulates later than and in different dystrophic neurites from BACE1, and that *Inpp5d* deficiency likely affects the mechanism specific to p-tau deposition.

Inpp5d haplodeficiency showed a minor or partial rescue effect on DAM transition in Tyrobp-deficient NLGF mouse microglia

Transcriptomic changes of microglia have been implicated in the progression of amyloid pathology. We performed RNA-seq on isolated microglia from *NLGF*, *Inpp5d*$^{+/-}$*;NLGF*, *Tyrobp*$^{-/-}$*;NLGF*, and *Inpp5d*$^{+/-}$*;Tyrobp*$^{-/-}$*;NLGF* mice at 9 months of age. Clustering analysis was performed using TCC-GUI[59] (Figure 6A). Whereas *Trem2*-dependent gene expression has been extensively analyzed using microglia isolated from β-amyloidosis mice,[20,27,60] transcriptional changes in *Tyrobp*-deficient mice have only been assessed by bulk tissue RNA-seq.[46,61] Therefore, we first analyzed the expression profiles of microglia from *Tyrobp*$^{-/-}$*;NLGF* mice. Among the 1,823 differentially expressed genes (DEGs; > 2-fold change, adjusted p value: <0.05), 1,258 genes were upregulated and 565 genes were downregulated (Figure 6B). The upregulated genes included *S100a8* and *S100a9* (associated with the inflammatory response), and *Clec4e* (C-type lectin). The downregulated genes included *Ch25h* (cholesterol metabolism), *Mamdc2* (regulation of the MAPK signaling pathway), *Spp1* (cytokine), *Dkk2*, and *Fzd9* (WNT signaling), which were the same as those identified in microglia of *Trem2*-deficient β-amyloidosis mice.[20,60] Of note, *Trem2*-dependent stage 2 DAM signature genes[27] were enriched in the downregulated genes (e.g., *Clec7a*, *Cst7*, *Itgax*, *Lpl*, and *Spp1*), supporting the essential role of TYROBP in conversion of homeostatic microglia into DAM. Furthermore, GO terms enriched in the downregulated genes included "cholesterol metabolic process" and "positive regulation of cell migration" (Figure S5A), consistent with a previous

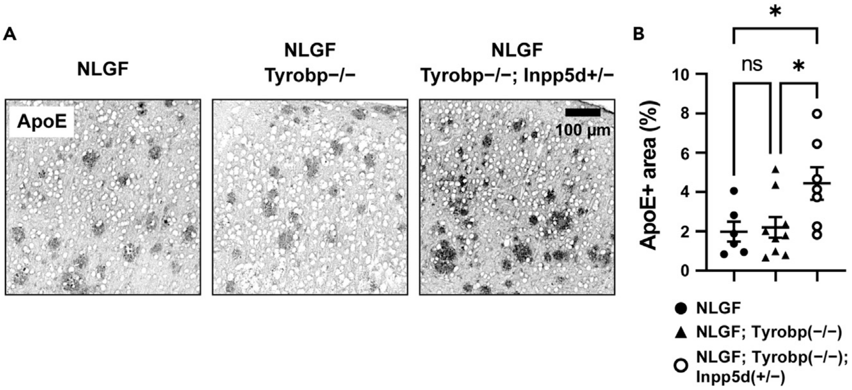

Figure 3. Inpp5d haplodeficiency increased ApoE deposition around amyloid plaques in Tyrobp-deficient NLGF mice

(A) Representative images of ApoE staining around the somatosensory cortex. Scale bar: 100 μm.

(B) Quantification of the ApoE-positive area (%) per unit area of the cortex (N = 6–9). Each point represents an individual mouse. Bars represent the mean ± SEM of all analyzed animals in each genotype. Male mice at 11–12 months of age were analyzed. One-way ANOVA followed by Tukey's multiple comparisons. ns: not significant ($p > 0.05$), $^*p < 0.05$.

study on *Trem2*-deficient microglia.[62] Moreover, "positive regulation of phosphatidylinositol 3-kinase signaling" was also identified in our dataset (Figures S3A and S5A). Collectively, *Tyrobp* deficiency causes transcriptional changes of microglia in a similar manner to those observed in *Trem2*-deficient microglia.

We then investigated the effects of *Inpp5d* haplodeficiency on the transcriptional profile of microglia in *Tyrobp*$^{-/-}$;*NLGF* mice. Among the 870 DEGs (>2-fold change, adjusted p value: <0.05), 306 genes were upregulated, whereas 564 were downregulated. We observed that *Tyrobp*$^{-/-}$;*NLGF* mice have more P2RY12-positive "homeostatic" microglia compared with *NLGF* mice, and this defect was corrected by additional deletion of *Inpp5d* (Figure S3E). We therefore asked whether *Inpp5d* reduction would restore DAM gene expression in *Tyrobp*-deficient mice. However, *Inpp5d*$^{+/-}$;*Tyrobp*$^{-/-}$;*NLGF* microglia showed almost no difference in DAM gene expression compared with *Tyrobp*$^{-/-}$;*NLGF* microglia (Figure 6C). Exceptions included *Lpl* and *Spp1*, although their increases were subtle. Some of the results were validated by qRT-PCR (Figure 6D). Immunohistochemical analyses of CD11c and Tmem119, a marker for DAM and homeostatic microglia, respectively, indicated that microglia from *Tyrobp*$^{-/-}$;*NLGF* and *Inpp5d*$^{+/-}$;*Tyrobp*$^{-/-}$;*NLGF* mice showed similar defects in the transition to the DAM phenotype (Figures 6E and 6F). These data suggest that *Inpp5d* haplodeficiency in *Tyrobp*$^{-/-}$;*NLGF* mice has a minor or partial effect on the acquisition of the DAM phenotype by microglia.

To obtain molecular insights into the beneficial role of *Inpp5d* haplodeficiency in *Tyrobp*$^{-/-}$;*NLGF* microglia, we compared DEGs between *Tyrobp*$^{-/-}$;*NLGF* and *Inpp5d*$^{+/-}$;*Tyrobp*$^{-/-}$;*NLGF* microglia. *Trem2* levels were similar among all the genotypes (Figure S5B), suggesting that the observed rescue effects were not explained by *Trem2* upregulation. The top five upregulated genes were *Wdfy1*, *Sox13*, *Fzd9*, *Mamdc2*, and *Pdcd1*, whereas the top five downregulated genes were *Neil3*, *Klrb1f*, *Slc25a31*, *Gm38248*, and *Xkr9* (Figure 6G). Among them, *Fzd9* and *Mamdc2* were downregulated by *Tyrobp* deficiency in the microglia of *NLGF* mice, as well as in the microglia of *Trem2*-deficient PS2APP mice.[20] *Fzd9* encodes a receptor for WNT,[63] which modulates the TREM2/TYROBP signaling pathway.[44] *Mamdc2*, a gene upregulated in AD model mouse microglia, is involved in type-I interferon response.[64] *Pdcd1* (also known as PD-1), upregulated in plaque-associated microglia, regulates Aβ phagocytosis as well as inflammatory responses.[65] *Wdfy1* modulates Toll-like receptor signaling,[66] which is also regulated by INPP5D.[67] These molecules may therefore contribute to the beneficial effects of *Inpp5d* haplodeficiency through their signaling pathways.

INPP5D negatively regulates the PI3K/AKT pathway in Tyrobp-deficient microglia

To ask how INPP5D reduction exerts its effect independently of the transcriptional change induced by TREM2 and TYROBP, we investigated its role in PI(3,4,5)P_3 signaling by assessing the phosphorylation of AKT[44] as indicative of PI(3,4,5)P_3 level. Phosphorylation level of AKT was reduced by *Trem2* or *Tyrobp*

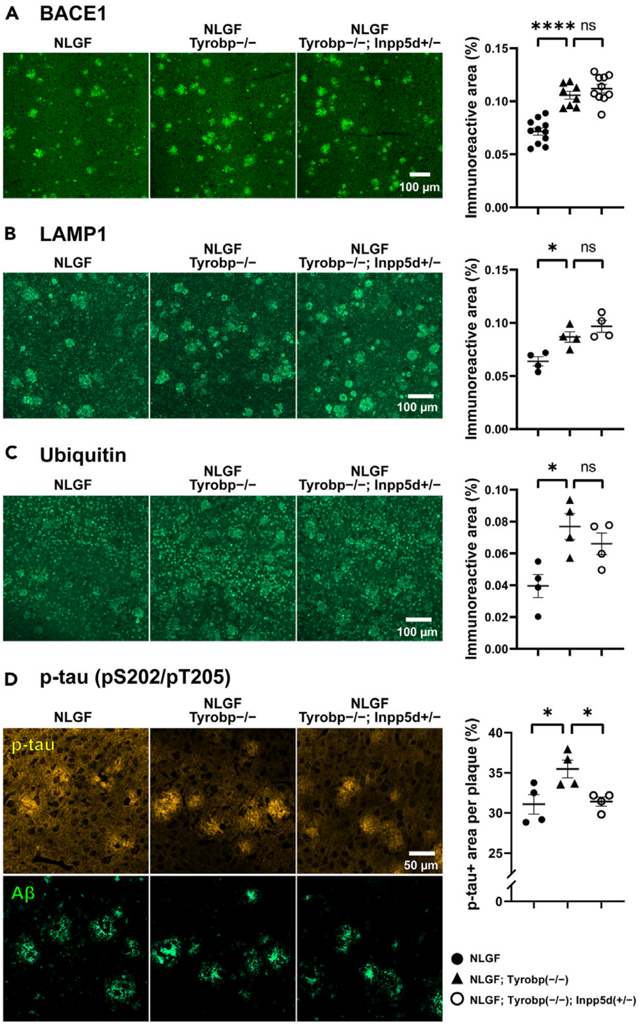

Figure 4. Inpp5d haplodeficiency attenuated p-tau accumulation in the dystrophic neurites of Tyrobp-deficient NLGF mice

(A–C) Representative staining for BACE1 (*A*, N = 8–11), LAMP1 (*B*, N = 4), and ubiquitin (*C*, N = 4) in the cortex from 9-month-old mice of the indicated genotypes. Quantifications of the immunoreactive area (% of cortical area) are shown in *right*. Note that, for ubiquitin, the plaque-associated signal was specifically quantified after excluding smaller particles corresponding to nucleus-localized physiological ubiquitin. Scale bars: 100 μm.

(D) Immunohistochemistry for p-tau (*yellow*) and Aβ (*green*) in a cortical region from 9-month-old mice of the indicated genotypes. The overlapping area of p-tau and Aβ signals was expressed as relative to the Aβ-positive area as 100% (N = 4). Scale bar: 50 μm. Each point represents an individual mouse. Bars represent the mean ± SEM of all analyzed animals in each genotype. One-way ANOVA followed by Tukey's multiple comparisons. ns: not significant ($p > 0.05$), *$p < 0.05$, ****$p < 0.0001$.

knockdown (KD) (Figures 7A and 7B), as well as *Tyrobp* deficiency in primary microglia (Figures S6A and S6B), whereas it was increased by *Inpp5d* KD. More relevant to *in vivo* situation, additional KD of *Inpp5d* corrected *p*-AKT levels in *Trem2* or *Tyrobp* KD cells (Figures 7A and 7B), and the similar results were observed in *ex vivo* microglia isolated from *Inpp5d*$^{+/-}$;*Tyrobp*$^{-/-}$;*NLGF* mice, although it did not reach a statistical significance (Figure S6C). These suggest that TREM2/TYROBP and INPP5D oppositely regulate PI(3,4,5)P_3 levels. Meanwhile, phosphorylation of phospholipase C-γ2 (PLCγ2), a protein activated downstream of PI(3,4,5)P_3,[68–71] was also reduced by *Trem2* or *Tyrobp* KD, but was not affected by *Inpp5d* (Figures 7A and 7B). This result can be explained by the fact that PLCγ2 activation requires not only PI(3,4,5)P_3 but also other upstream inputs (i.e., SYK activation). Phosphorylation levels of ERK1 and ERK2 were affected similarly to that of PLCγ2 (Figures S6D and S6E), consistent with that MAPK is regulated

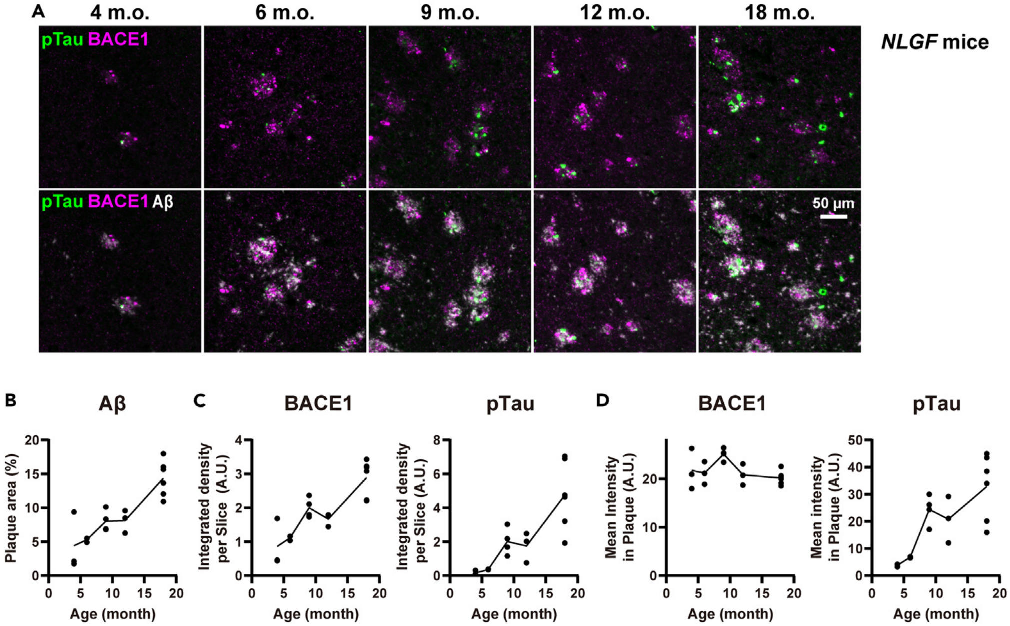

Figure 5. Differential accumulation of p-tau and BACE1 in dystrophic neurites

(A–D) Triple labeling of p-tau (*A*, *green*), BACE1 (*magenta*), and Aβ (*gray*) in the brain sections from 4-, 6-, 9-, 12-, and 18-month-old (m.o.) female *NLGF* mice, around amygdala (*A*, Scale bar: 50 μm). The Aβ-positive area (% of brain section, *B*), and the overall fluorescent signals of BACE1 and p-tau per section (*C*) were elevated with aging. Of note, the mean intensity of BACE1 in plaques was relatively constant from as early as 4 months old, in contrast to p-tau being stronger with aging (*D*, N = 3–6). Each point represents an individual mouse.

independently of PI3K pathway. Considering that PI3K/AKT sits upstream of mTORC/autophagy, we also examined an autophagy marker LC3B (Figures S6F and S6G). *Trem2* or *Tyrobp* KD increased the level of LC3B in its lipidated form, suggesting that reduced PI3K activity unlocks autophagy.[25] In contrast, *Inpp5d* KD reduced LC3B-II levels, but the effect was modest. The minor contribution of INPP5D to autophagy regulation is likely due to the existence of multiple PI(3,4,5)P_3 phosphatases in the cell.

We further asked the role of other PI(3,4,5)P_3 phosphatases, namely, inositol polyphosphate phosphatase-like 1 (INPPL1; a closest homolog of INPP5D) and phosphatase and tensin homolog,[38] as well as PI(3,4)P_2 phosphatases, inositol polyphosphate-4-phosphatase type I A and type II B, as they also contribute to AKT activation[72] (Figure 7C). Interestingly, the ability to revert the reduced *p*-AKT in *Tyrobp* KD cells was unique to *Inpp5d* and not seen by the other phosphatases KD (Figures 7D and 7E). Simultaneous KD of *Inppl1* with *Inpp5d* also did not modulate the effect of single *Inpp5d* KD, indicating that *Inppl1* does not compensate for the lack of *Inpp5d* function. These data indicate a unique inhibitory role of INPP5D in the PI3K/AKT pathway.

While our finding that INPP5D antagonizes PI(3,4,5)P_3 function and its inhibitory effect does not require TYROBP (Figure 1), a previous study suggests that INPP5D also inhibits PI3K activation by binding to TYROBP, preventing its interaction with SYK.[40] We thus examined the interaction between INPP5D and TYROBP. Their binding was unexpectedly not captured by co-immunoprecipitation of HEK293 expressing TREM2, TYROBP, and INPP5D (Figure S6H). However, *in situ* proximity ligation assay[73] of primary microglia indicated that INPP5D is in proximity (<30 nm) with TREM2 (Figures S6I and S6J) and TYROBP (Figure S6K). A specific interaction between TREM2 and SYK was also observed, which was enhanced by *Inpp5d* KD (Figure S6L), suggesting that INPP5D inhibits SYK activation process, probably by competitively binding to TREM2. These suggest that INPP5D regulates microglial function via multiple mechanisms that converge on PI(3,4,5)P_3 downregulation.

Considering that an AD risk variant of *INPP5D* (*rs35349669*) reportedly increases *INPP5D* expression,[39] we asked the effect of INPP5D overexpression in microglia. In murine MG6 cell line, phosphorylation of AKT

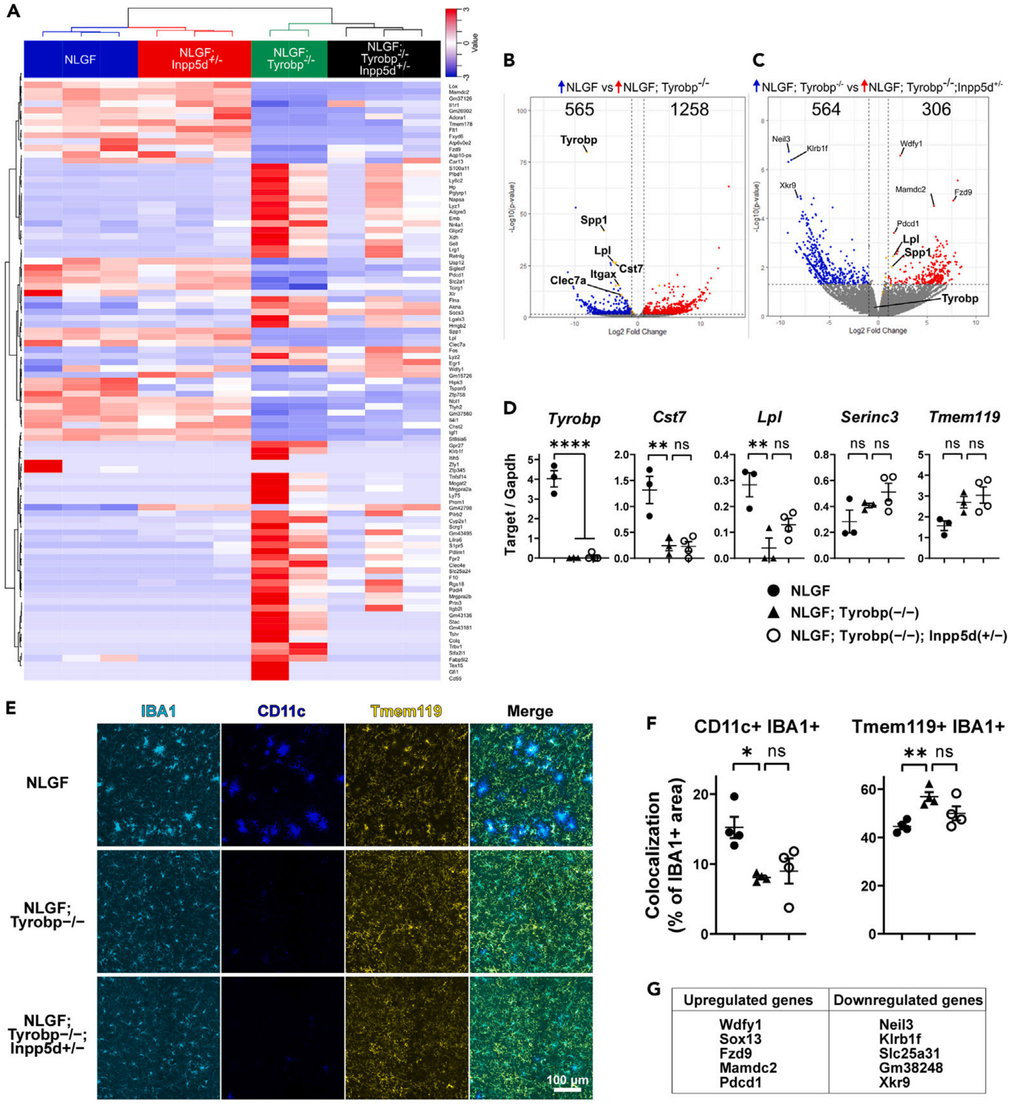

Upregulated genes	Downregulated genes
Wdfy1 Sox13 Fzd9 Mamdc2 Pdcd1	Neil3 Klrb1f Slc25a31 Gm38248 Xkr9

Figure 6. RNA-seq analyses of Inpp5d- and/or Tyrobp-deficient NLGF mice

(A) RNA-seq data of isolated microglia from 9-month-old mice were analyzed by TCC-GUI. Top 100 genes were shown in a heatmap, in which color indicates the relative expression level. Canberra distances were used to perform the clustering analysis.

(B) Volcano plot of *Tyrobp*$^{-/-}$;*NLGF* versus *NLGF*. The negative log10 transformed p values are plotted against the log2-fold changes. The upregulated genes in *Tyrobp*$^{-/-}$;*NLGF* microglia were colored in *red*, while the downregulated genes were in *blue*.

(C) Volcano plot of *Inpp5d*$^{+/-}$;*Tyrobp*$^{-/-}$;*NLGF* versus *Tyrobp*$^{-/-}$;*NLGF*. The negative log10 transformed p values are plotted against the log2-fold changes. The upregulated genes in *Inpp5d*$^{+/-}$;*Tyrobp*$^{-/-}$;*NLGF* microglia were colored in *red*, while the downregulated genes were in *blue*.

(D) Validation of RNA-seq data by qRT-PCR. mRNA expressions of *Tyrobp*, *Cst7*, *Lpl*, *Serinc3*, and *Tmem119* in isolated microglia were shown by normalizing to *Gapdh*.

(E and F) Immunohistochemistry for IBA1 (*E*, *cyan*), CD11c (*blue*), and Tmem119 (*yellow*) in the cortical region. The overlapping area of IBA1/CD11c (*F*, *left*) or IBA1/Tmem119 (*right*) staining was shown as relative to the IBA1-positive area as 100%. Scale bar: 100 μm.

(G) Top 5 genes of upregulated or downregulated in *Inpp5d*$^{+/-}$;*Tyrobp*$^{-/-}$;*NLGF* microglia compared with *Tyrobp*$^{-/-}$;*NLGF* microglia. Each point represents an individual mouse. Bars represent the mean ± SEM of all analyzed animals in each genotype. One-way ANOVA followed by Tukey's multiple comparisons. ns: not significant ($p > 0.05$), $^{*}p < 0.05$, $^{**}p < 0.01$, $^{****}p < 0.0001$. See also Figure S5.

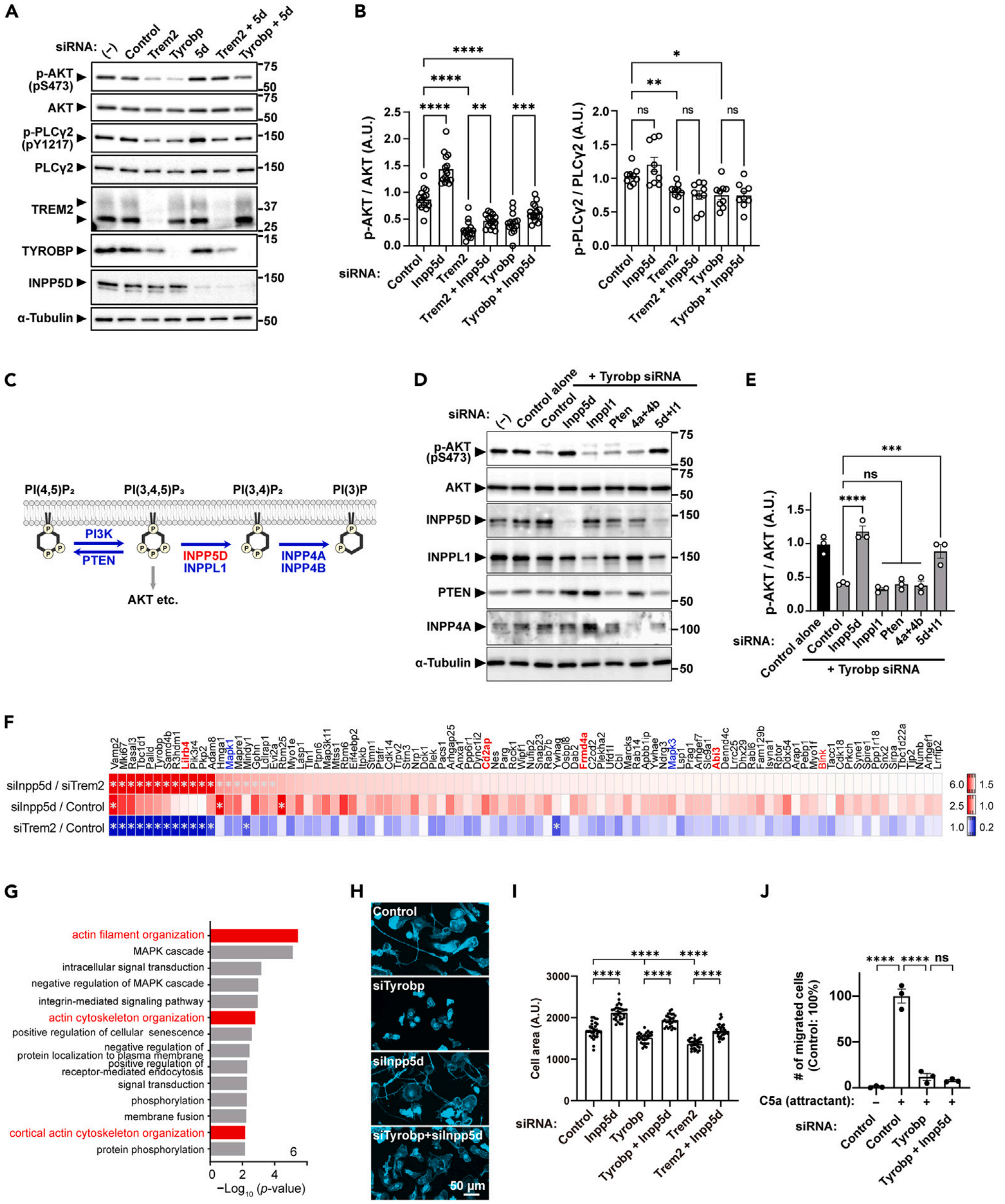

Figure 7. Inpp5d reduction upregulated *p*-AKT levels and promoted cell adhesion in Tyrobp KD cells

(A and B) Effects of *Trem2*, *Tyrobp*, or *Inpp5d* KD on the phosphorylation levels of AKT and PLCγ2 in primary microglia (*A*). The levels of *p*-AKT (*B*, *left*, N = 15) and *p*-PLCγ2 (*right*, N = 9) were shown as relative to the total levels of AKT and PLCγ2, respectively.

(C) Schematic of PI(3,4,5)P_3 metabolisms and related enzymes.

(D and E) Effects of simultaneous KD of *Tyrobp* and phosphoinositide phosphatases (*D*). The *p*-AKT level was shown as relative to the total AKT level (*E*, N = 3).

(F and G) Phosphoproteomic analysis of primary microglia treated with siRNA against *Trem2* and *Inpp5d*. Indicated are phosphoproteins whose expression levels (log2-transformed fold-change relative to the non-target siRNA control value) are oppositely regulated by *Inpp5d* and *Trem2* (*Inpp5d* vs *Trem2* > 1.5, *Inpp5d* vs non-target siRNA >1, *Trem2* vs non-target siRNA <1). Their relative levels were color-coded in the heatmap (*F*). Asterisks indicate statistical significance (adjusted p value <0.05). Note that the list includes the proteins with sub-threshold p value (p > 0.05). The GO term enrichment analysis of the 94 proteins were shown in *G*.

(H and I) Representative images of siRNA-transfected primary microglia on glass coverslips after brief exposure to lipopolysaccharides (*H*, scale bar: 50 µm). Quantification of the cell area was shown in *I*.

Figure 7. *Continued*

(J) Transwell assay of siRNA-transfected primary microglia toward C5a. The number of migrated cells was shown by normalizing to the control siRNA-transfected, C5a-treated group as 100%. Each point represents an individual trial. Bars represent the mean ± SEM of all analyzed trials in each condition. One-way ANOVA was used except for *B* using repeated measures one-way ANOVA, followed by Tukey's multiple comparisons. ns: not significant ($p > 0.05$), *$p < 0.05$, **$p < 0.01$, ***$p < 0.001$, ****$p < 0.0001$. See also Figure S6.

was increased upon agonist antibody for TREM2 (Figures S6M and S6N); however, its level was unchanged by overexpressing wild-type or phosphatase-dead mutant of INPP5D, suggesting that simple overexpression of INPP5D is not enough to affect PI(3,4,5)P_3 pathway. Importantly, a previous report suggests that INPP5D activation requires a conformational change to overcome an autoinhibitory intramolecular interaction.[74] Of note, *rs35349669* is located near internal transcription start site predicted to yield a truncated isoform of INPP5D[75] and may affect the autoinhibition mechanism. It is therefore important to explore the consequence of this variant in future studies.

INPP5D negatively regulates actin remodeling and cellular adhesion of microglia

To further gain insight into the role of INPP5D in microglial regulation, we looked for proteins that are affected similarly to AKT. For this purpose, phosphoproteins of primary microglia treated with siRNA against *Trem2* or *Inpp5d* were enriched and subjected to phosphoproteomic analysis. Considering an expected high off-target activity of siRNA, we only focused on phosphoproteins whose abundance is oppositely regulated by *Trem2* and *Inpp5d*, rather than those that are affected by each of them (i.e., *Inpp5d* vs *Trem2* > 1.5, *Inpp5d* vs non-target siRNA >1, *Trem2* vs non-target siRNA <1 in log2-transformed fold-change). However, the phosphoproteins with significant change in abundance (adjusted p value <0.05) were limited, and pathway enrichment analysis was not possible. We therefore looked at proteins with sub-threshold p values (Figure 7F). This criterion unfortunately did not lead to AKT identification possibly due to its low abundance but is nevertheless reliable since it found MAPK1/ERK2 and MAPK3/ERK1, for both of which we observed that the phosphorylation levels were increased by KD of *Trem2* compared with *Inpp5d* (Figures S6D and S6E). The GO term enrichment analysis of the resultant 94 proteins indicated "actin filament organization" as the most significant (Figure 7G). In addition, the list included multiple AD risk factors (LILRB4, CD2AP, FRMD4A, ABI3, and BLNK), among which CD2AP and ABI3 are involved in the actin remodeling process. The finding of ABI3 is particularly interesting, since its deficiency in β-amyloidosis mice causes microglial dissociation from plaques.[76]

Given that TREM2 and INPP5D oppositely regulate protein phosphorylation related to actin remodeling process, we asked whether they are involved in actin-related functions of primary microglia. Because *Inpp5d* reduction affects microglial association with plaques *in vivo*, we first examined its role in cell adhesion. We noticed that *Trem2* or *Tyrobp* KD caused a significant reduction of cell area on glass coverslips, particularly when briefly primed with lipopolysaccharide to mimic an *in vivo* inflammatory state (Figure 7H), indicating impaired cell adhesion. Interestingly, simultaneous KD of *Inpp5d* restored the defects (Figure 7I), suggesting that TREM2/TYROBP and INPP5D oppositely regulate cell adhesion. Next, we examined the effects on chemotaxis and cell proliferation/survival, since their deficits are implicated in the defective plaque association of *Trem2*-deficient microglia.[11,77,78] Chemotaxis to C5a, a potent chemoattractant of microglia, was indeed affected by *Tyrobp* KD, but was not reverted by *Inpp5d* KD (Figure 7J). Similarly, *Inpp5d* KD did not rescue the reduced viability of *Trem2* or *Tyrobp* KD cells (Figure S6O), consistent with *in vivo* data (Figure 1H). Based on these observations, *Inpp5d* reduction specifically increases cell adhesion, which likely underlies the enhanced plaque association of microglia observed *in vivo*.

DISCUSSION

In the present study, we investigated the pathological role of *INPP5D*, an AD risk gene expressed in microglia. *Inpp5d* haplodeficiency in *NLGF* mice did not affect Aβ deposition, gliosis, or neurite dystrophy. However, in *Tyrobp*-deficient *NLGF* mice showing TREM2 loss-of-function phenotypes, *Inpp5d* haplodeficiency restored microglial envelopment of plaques, altered plaque morphology, increased astrocyte activation, and reduced p-tau levels in dystrophic neurites. RNA-seq of isolated microglia and immunohistochemical analyses suggest that *Inpp5d* reduction has a minor or partial effect on the DAM transition of *Tyrobp*-deficient *NLGF* mouse microglia. Instead, KD experiments revealed that INPP5D has unique inhibitory roles in cell adhesion as well as in PI(3,4,5)P_3 signaling. Collectively, *Inpp5d* haplodeficiency alleviates the detrimental effects of *Tyrobp* deficiency in microglia, thereby affecting p-tau deposition around Aβ plaques.

TREM2 is crucial for microglia to cluster around plaques and thereby protect neurons from amyloid toxicity. TREM2 regulates multiple aspects of microglial function, including cell proliferation/survival, energy metabolism, and transformation into DAM[11,25,27]; however, which factor contributes to the protective effect remains unclear. Ulland et al. reported that metabolic correction of *Trem2*-deficient mice by cyclocreatine restores the microglial envelopment of plaques and ameliorates neurite dystrophy.[25] Similarly, we showed that INPP5D reduction in *Tyrobp*-deficient *NLGF* mice restores the microglial clustering and attenuates p-tau deposition, suggesting that physical interaction between microglia and plaques limits the p-tau deposition around plaques. On the other hand, the neuroprotective effects other than p-tau were not evident in our mice, suggesting that signaling pathways other than the PI3K pathway are required for this process.

Inpp5d haplodeficiency in *Tyrobp*$^{-/-}$;*NLGF* mice did not significantly alter brain Aβ deposition, although it increased microglial association with Aβ plaques. While this may be due to the lack of a functional TREM2 receptor, two recent studies (published after the initial submission of our manuscript) have questioned the role of INPP5D in Aβ clearance using similar *Inpp5d*-deficient β-amyloidosis mice.[79,80] In fact, these studies report conflicting results regarding Aβ pathology, which may be due to differences in the mouse models (NLGF, APP/PS1, and 5xFAD) and detection methods used. However, it is interesting to note that homozygous deletion of *Inpp5d* in APP/PS1 mice does not reduce Aβ burden, and the increased microglial association with plaques in these mice does not appear to be sufficient to enhance Aβ clearance by microglia.[79] While studies in *Trem2* knockout mice suggest the importance of plaque-associated microglia in Aβ clearance,[11,51] pharmacological depletion of microglia in various β-amyloidosis mice did not increase Aβ deposition,[52,81] and thus the precise role of microglia in Aβ metabolism remains unclear. On the other hand, the loss of plaque-associated microglia in these studies was consistently associated with impaired plaque compaction, and plaques with different morphologies have different effects on surrounding neurons.[17,18,20,52] Since *Inpp5d* reduction alters plaque morphology to a compact shape in *Tyrobp*-deficient *NLGF* mice, the beneficial effect of *Inpp5d* deficiency may be due to the improvement of plaque compaction as well as the physical barrier around the plaques.

Microglial envelopment of plaques suppresses periplaque neuronal dystrophy, which likely underlies the mechanism that TREM2 restrains the Aβ-mediated enhancement of p-tau accumulation.[22,23] Our findings that *Inpp5d* reduction in *Tyrobp*-deficient *NLGF* mice specifically mitigates p-tau deposition, and that p-tau accumulates later than and in different neurites from BACE1 suggest that INPP5D targets a putative-specific mechanism of p-tau deposition, which may be driven by cumulative damage in neurites, or by some neurotoxic factors that increase late in plaque accumulation. Among such candidates, Aβ oligomers disrupt microtubules in nearby axons,[82] thereby contributing to cytosolic release of tau, and its phosphorylation and aggregation.[21] Considering that microglia restrain the diffusion of Aβ oligomers around plaques,[55] INPP5D may affect their diffusion by strengthening the contact with plaques. On the other hand, *Inpp5d* haplodeficiency in *Tyrobp*-deficient *NLGF* mice did not increase plaque-associated microglia or fully restore the plaque morphology, which may be further required to ameliorate the deposition of other markers.

GFAP-positive reactive astrocytes were dramatically reduced in *Tyrobp*-deficient *NLGF* mice, reminiscent of the phenotype of *Trem2* deficiency or CSF1R inhibition,[20,51,52,83] indicating an essential role of microglia in the induction of reactive astrocytes. Microglia contribute to neurotoxic astrocyte formation upon inflammatory stimuli.[48] In addition, Aβ abundance in the brain is related to the GFAP elevation in preclinical AD.[84,85] These suggest that microglia and Aβ coordinately lead astrocyte activation. Here, we found that *Inpp5d* reduction restored astrocyte activation in *Tyrobp*-deficient *NLGF* mice, suggesting the importance of the physical interaction of microglia with plaques or PI(3,4,5)P_3 signaling in this process.

Our RNA-seq results provided molecular insights into the phenotypes observed in this study. For the first time to our knowledge, we profiled the transcriptional changes of microglia in *Tyrobp*-deficient β-amyloidosis mice. The DEGs in *Tyrobp*-deficient microglia quite resemble those described in *Trem2*-deficient microglia, in agreement with assumption that TYROBP is essential for TREM2 function regulating the transition of microglia into the DAM state. Interestingly, a recent study on *Inpp5d*$^{\text{flox/flox}}$;*Cx3cr1-CreER*;APP/PS1 mice suggests that *Inpp5d* deficiency facilitates the transition to a DAM-like state in microglia,[79] but *Inpp5d* reduction in *Tyrobp*-deficient mice shows little or partial effect on DAM gene expression, suggesting that multiple TYROBP-mediated signaling pathways, not just the

PI3K pathway, are required for this process. Furthermore, *Inpp5d* reduction caused the transcriptional upregulation of *Wdfy1*, *Sox13*, *Fzd9*, *Mamdc2*, and *Pdcd1*, and the downregulation of *Neil3*, *Klrb1f*, *Slc25a31*, *Gm38248*, and *Xkr9*. Future studies should address their roles in the amyloid recognition/association process as well as the p-tau deposition.

One primary phenotype oppositely regulated by TREM2/TYROBP and INPP5D was the cell adhesion activity, which correlated with the altered phosphorylation of proteins that are involved in actin assembly. The reduced cell adhesion of *Trem2* KD microglia is likely linked to the reported defects in cytoskeletal organization,[86] as well as the surface expression of β-integrins.[87] Intriguingly, PI(3,4,5)P_3 regulates actin polymerization and integrin activation[38]; and β1-integrin is implicated in Aβ recognition by microglia.[88] Furthermore, previous studies showed that microglia have a physical contact with plaques in a TREM2/TYROBP-dependent manner[18,55] and that microglia lacking the contact were not able to make plaques into compact shapes nor protect neurons,[89] highlighting the importance of the physical contact. We therefore speculate that the enhanced adhesion by *Inpp5d* haplodeficiency would increase the physical contact with plaques and strengthen the neuroprotective function by microglia.

TREM2/TYROBP and INPP5D exert opposing effects on the PI(3,4,5)P_3 downstream signaling. While INPP5D may exert this effect via the PI(3,4,5)P_3 dephosphorylating activity, our PLA results suggest a different inhibitory role in the TYROBP-SYK interaction, which is quite reminiscent of the previous finding that INPP5D inhibits SYK/PI3K activation by competitively binding to TYROBP.[40] Given the central role of SYK in the TREM2-mediated microglial signaling pathway,[90,91] it is interesting to investigate whether INPP5D inhibition enhances SYK activity. On the other hand, we also found that INPP5D reduction upregulates PI(3,4,5)P_3 signaling in the absence of TYROBP, suggesting that INPP5D plays a role in the metabolism of a PI(3,4,5)P_3 pool that is presumably generated by other upstream receptors that activates PI3K. Interestingly, PI(3,4,5)P_3 phosphatases other than INPP5D (*Pten* and *Inppl1*) were not involved in *p*-AKT regulation in *Tyrobp* KD cells. This raises the interesting possibility that the PI(3,4,5)P_3 pool targeted by INPP5D has a specific role in the AKT activation. Further studies are required to elucidate the underlying mechanism and the different roles of the phosphatases in this pathway.

A common variant of the INPP5D gene (rs35349669) is associated with an increased risk of late-onset AD.[2] While its effect on INPP5D function remains unclear, rs35349669 was associated with higher p-tau levels in the cerebrospinal fluid (CSF) of patients with AD.[92] Altered CSF tau was also reported for other INPP5D variants,[93,94] suggesting a link between INPP5D and p-tau deposition. Moreover, the potential role of INPP5D in the Aβ and tau crosstalk may provide a unique opportunity for AD therapy. INPP5D inhibitors may be beneficial to prevent tau deposition. Nonetheless, complete inhibition of INPP5D can cause an adverse effect particularly in peripheral tissues,[43] and therefore it is necessary to develop a specific way to target it in microglia. For this purpose, it would be important to identify a microglia-specific regulator of INPP5D. Of note, INPP5D is upregulated near Aβ plaques[42] in an unknown mechanism, which may involve druggable targets to regulate microglial expression of INPP5D. Such drugs would provide a novel microglia-targeting therapeutic/preventive approach for AD, specifically against Aβ-driven worsening of tau deposition.

Limitations of the study

Our findings on the beneficial effects of *Inpp5d* reduction were mainly obtained from a *Tyrobp*-deficient, TREM2 loss-of-function mouse model. To know the potential beneficial effect of INPP5D inhibition as an AD therapeutic, it would be helpful to analyze the single knockout effect of *Inpp5d* in AD model animals, preferably using multiple biological assays, including biomarker tests, electrophysiological analyses, and behavioral tests.

STAR★METHODS

Detailed methods are provided in the online version of this paper and include the following:

- KEY RESOURCES TABLE
- RESOURCE AVAILABILITY
  - Lead contact
  - Materials availability
  - Data and code availability

- EXPERIMENTAL MODEL AND SUBJECT DETAILS
  - Mice
  - Primary microglia culture
- METHOD DETAILS
  - Brain sample collection and preparation
  - Histochemistry on free-floating brain sections
  - Immunohistochemistry on paraffin-embedded sections
  - Brain Aβ measurement by ELISA
  - Isolation of microglia from adult mouse brain
  - Sample preparation for immunoblotting
  - Immunoblotting
  - Transfection of primary microglia
  - Phosphoproteomic analysis of primary microglia
  - Adhesion assay of primary microglia
  - Chemotaxis assay of primary microglia
  - alamarBlue assay of primary microglia
  - Co-immunoprecipitation experiment
  - *In situ* proximity ligation assay
  - INPP5D overexpression in MG6 cells and antibody-mediated stimulation of TREM2
  - RNA sequencing
  - qRT-PCR
  - Image acquisition and analysis
- QUANTIFICATION AND STATISTICAL ANALYSIS

SUPPLEMENTAL INFORMATION

Supplemental information can be found online at https://doi.org/10.1016/j.isci.2023.106375.

ACKNOWLEDGMENTS

The authors appreciate our current and previous laboratory members for helpful discussions and thank Keiko Mutsuura and Natsuki Dohi (Nagoya City University) for preparing paraffin-embedded sections, and Kaoru Yamada (The University of Tokyo) for technical assistance of animal experiments. We are also grateful to Imaging Core Laboratory (The Institute of Medical Science, The University of Tokyo), Yasuo Uchiyama and Hiroyuki Hioki (Juntendo University) for image acquisition using Dragonfly microscopies. This work was supported in part by Biogen (to T. Tomita), the Mitsubishi Foundation (to T. Tomita), the Uehara Memorial Foundation (to T. Tomita), Grants-in-Aid for Scientific Research (A) (15H02492, 19H01015 to T. Tomita), grant-in-aid for Scientific Research (C) (19K07080 to S.T.) from the Japan Society for the Promotion of Science, Strategic Research Program for Brain Sciences from the Japan Agency for Medical Research and Development (JP20dm0107056, JP20dm0207073 to T. Tomita and S.T.), Moonshot R&D from Japan Science and Technology Agency (JPMJMS2024 to T. Tomita), World-leading Innovative Graduate Study Program for Life Science and Technology from the University of Tokyo (to A.I.). A.I. receives a research fellowship for young scientists from the Japan Society for the Promotion of Science.

AUTHOR CONTRIBUTIONS

Conceptualization, S.T.; Methodology, S.T., A.I., G.I., Y.H., and T.I.; Investigation, A.I., S.T., S.K., H.M., K.W., H.E., and H.S.; Resources, J.S., T. Sasaki, T. Saito, T.C.S., and T. Takai; Writing – Original Draft, S.T., A.I., T.I., and T. Tomita; Funding Acquisition, S.T. and T. Tomita; Supervision, T. Tomita.

DECLARATION OF INTERESTS

The authors declare no competing interests.

Received: February 8, 2023
Revised: February 24, 2023
Accepted: March 7, 2023
Published: March 13, 2023

REFERENCES

1. Jansen, I.E., Savage, J.E., Watanabe, K., Bryois, J., Williams, D.M., Steinberg, S., Sealock, J., Karlsson, I.K., Hägg, S., Athanasiu, L., et al. (2019). Genome-wide meta-analysis identifies new loci and functional pathways influencing Alzheimer's disease risk. Nat. Genet. *51*, 404–413. https://doi.org/10.1038/s41588-018-0311-9.
2. Lambert, J.-C., Ibrahim-Verbaas, C.A., Harold, D., Naj, A.C., Sims, R., Bellenguez, C., DeStafano, A.L., Bis, J.C., Beecham, G.W., Grenier-Boley, B., et al. (2013). Meta-analysis of 74,046 individuals identifies 11 new susceptibility loci for Alzheimer's disease. Nat. Genet. *45*, 1452–1458. https://doi.org/10.1038/ng.2802.
3. Takatori, S., Wang, W., Iguchi, A., and Tomita, T. (2019). Genetic risk factors for Alzheimer disease: emerging roles of microglia in disease pathomechanisms. In Advances in Experimental Medicine and Biology, pp. 83–116. https://doi.org/10.1007/978-3-030-05542-4_5.
4. Guerreiro, R., Wojtas, A., Bras, J., Carrasquillo, M., Rogaeva, E., Majounie, E., Cruchaga, C., Sassi, C., Kauwe, J.S.K., Younkin, S., et al. (2013). TREM2 variants in Alzheimer's disease. N. Engl. J. Med. *368*, 117–127. https://doi.org/10.1056/NEJMoa1211851.
5. Jonsson, T., Stefansson, H., Steinberg, S., Jonsdottir, I., Jonsson, P.V., Snaedal, J., Bjornsson, S., Huttenlocher, J., Levey, A.I., Lah, J.J., et al. (2013). Variant of TREM2 associated with the risk of Alzheimer's disease. N. Engl. J. Med. *368*, 107–116. https://doi.org/10.1056/NEJMOA1211103.
6. Ulrich, J.D., Ulland, T.K., Colonna, M., and Holtzman, D.M. (2017). Elucidating the role of TREM2 in Alzheimer's disease. Neuron *94*, 237–248. https://doi.org/10.1016/J.NEURON.2017.02.042.
7. Yeh, F.L., Hansen, D.V., and Sheng, M. (2017). TREM2, microglia, and neurodegenerative diseases. Trends Mol. Med. *23*, 512–533. https://doi.org/10.1016/J.MOLMED.2017.03.008.
8. Ulland, T.K., and Colonna, M. (2018). TREM2 — a key player in microglial biology and Alzheimer disease. Nat. Rev. Neurol. *14*, 667–675. https://doi.org/10.1038/s41582-018-0072-1.
9. Deczkowska, A., Weiner, A., and Amit, I. (2020). The physiology, pathology, and potential therapeutic applications of the TREM2 signaling pathway. Cell *181*, 1207–1217. https://doi.org/10.1016/J.CELL.2020.05.003.
10. Kleinberger, G., Yamanishi, Y., Suárez-Calvet, M., Czirr, E., Lohmann, E., Cuyvers, E., Struyfs, H., Pettkus, N., Wenninger-Weinzierl, A., Mazaheri, F., et al. (2014). TREM2 mutations implicated in neurodegeneration impair cell surface transport and phagocytosis. Sci. Transl. Med. *6*, 243ra86. https://doi.org/10.1126/scitranslmed.3009093.
11. Wang, Y., Cella, M., Mallinson, K., Ulrich, J.D., Young, K.L., Robinette, M.L., Gilfillan, S., Krishnan, G.M., Sudhakar, S., Zinselmeyer, B.H., et al. (2015). TREM2 lipid sensing sustains the microglial response in an Alzheimer's disease model. Cell *160*, 1061–1071. https://doi.org/10.1016/j.cell.2015.01.049.
12. Yeh, F.L., Wang, Y., Tom, I., Gonzalez, L.C., and Sheng, M. (2016). TREM2 binds to apolipoproteins, including APOE and CLU/APOJ, and thereby facilitates uptake of amyloid-beta by microglia. Neuron *91*, 328–340. https://doi.org/10.1016/j.neuron.2016.06.015.
13. Kober, D.L., Alexander-Brett, J.M., Karch, C.M., Cruchaga, C., Colonna, M., Holtzman, M.J., and Brett, T.J. (2016). Neurodegenerative disease mutations in TREM2 reveal a functional surface and distinct loss-of-function mechanisms. Elife *5*, e20391. https://doi.org/10.7554/eLife.20391.
14. Song, W., Hooli, B., Mullin, K., Jin, S.C., Cella, M., Ulland, T.K., Wang, Y., Tanzi, R.E., and Colonna, M. (2017). Alzheimer's disease-associated TREM2 variants exhibit either decreased or increased ligand-dependent activation. Alzheimers Dement. *13*, 381–387. https://doi.org/10.1016/j.jalz.2016.07.004.
15. Sudom, A., Talreja, S., Danao, J., Bragg, E., Kegel, R., Min, X., Richardson, J., Zhang, Z., Sharkov, N., Marcora, E., et al. (2018). Molecular basis for the loss-of-function effects of the Alzheimer's disease–associated R47H variant of the immune receptor TREM2. J. Biol. Chem. *293*, 12634–12646. https://doi.org/10.1074/jbc.RA118.002352.
16. Korvatska, O., Leverenz, J.B., Jayadev, S., McMillan, P., Kurtz, I., Guo, X., Rumbaugh, M., Matsushita, M., Girirajan, S., Dorschner, M.O., et al. (2015). R47H variant of TREM2 associated with Alzheimer disease in a large late-onset family: clinical, genetic, and neuropathological study. JAMA Neurol. *72*, 920–927. https://doi.org/10.1001/JAMANEUROL.2015.0979.
17. Wang, Y., Ulland, T.K., Ulrich, J.D., Song, W., Tzaferis, J.A., Hole, J.T., Yuan, P., Mahan, T.E., Shi, Y., Gilfillan, S., et al. (2016). TREM2-mediated early microglial response limits diffusion and toxicity of amyloid plaques. J. Exp. Med. *213*, 667–675. https://doi.org/10.1084/jem.20151948.
18. Yuan, P., Condello, C., Keene, C.D., Wang, Y., Bird, T.D., Paul, S.M., Luo, W., Colonna, M., Baddeley, D., and Grutzendler, J. (2016). TREM2 haplodeficiency in mice and humans impairs the microglia barrier function leading to decreased amyloid compaction and severe axonal dystrophy. Neuron *90*, 724–739. https://doi.org/10.1016/j.neuron.2016.05.003.
19. Song, W.M., Joshita, S., Zhou, Y., Ulland, T.K., Gilfillan, S., and Colonna, M. (2018). Humanized TREM2 mice reveal microglia-intrinsic and -extrinsic effects of R47H polymorphism. J. Exp. Med. *215*, 745–760. https://doi.org/10.1084/jem.20171529.
20. Meilandt, W.J., Ngu, H., Gogineni, A., Lalehzadeh, G., Lee, S.-H., Srinivasan, K., Imperio, J., Wu, T., Weber, M., Kruse, A.J., et al. (2020). Trem2 deletion reduces late-stage amyloid plaque accumulation, elevates the Aβ42:Aβ40 ratio, and exacerbates axonal dystrophy and dendritic spine loss in the PS2APP Alzheimer's mouse model. J. Neurosci. *40*, 1956–1974. https://doi.org/10.1523/JNEUROSCI.1871-19.2019.
21. He, Z., Guo, J.L., McBride, J.D., Narasimhan, S., Kim, H., Changolkar, L., Zhang, B., Gathagan, R.J., Yue, C., Dengler, C., et al. (2018). Amyloid-β plaques enhance Alzheimer's brain tau-seeded pathologies by facilitating neuritic plaque tau aggregation. Nat. Med. *24*, 29–38. https://doi.org/10.1038/nm.4443.
22. Leyns, C.E.G., Gratuze, M., Narasimhan, S., Jain, N., Koscal, L.J., Jiang, H., Manis, M., Colonna, M., Lee, V.M.Y., Ulrich, J.D., and Holtzman, D.M. (2019). TREM2 function impedes tau seeding in neuritic plaques. Nat. Neurosci. *22*, 1217–1222. https://doi.org/10.1038/s41593-019-0433-0.
23. Lee, S.-H., Meilandt, W.J., Xie, L., Gandham, V.D., Ngu, H., Barck, K.H., Rezzonico, M.G., Imperio, J., Lalehzadeh, G., Huntley, M.A., et al. (2021). Trem2 restrains the enhancement of tau accumulation and neurodegeneration by β-amyloid pathology. Neuron *109*, 1283–1301.e6. https://doi.org/10.1016/j.neuron.2021.02.010.
24. Pascoal, T.A., Benedet, A.L., Ashton, N.J., Kang, M.S., Therriault, J., Chamoun, M., Savard, M., Lussier, F.Z., Tissot, C., Karikari, T.K., et al. (2021). Microglial activation and tau propagate jointly across Braak stages. Nat. Med. *27*, 1592–1599. https://doi.org/10.1038/S41591-021-01456-W.
25. Ulland, T.K., Song, W.M., Huang, S.C.-C., Ulrich, J.D., Sergushichev, A., Beatty, W.L., Loboda, A.A., Zhou, Y., Cairns, N.J., Kambal, A., et al. (2017). TREM2 maintains microglial metabolic fitness in Alzheimer's disease. Cell *170*, 649–663.e13. https://doi.org/10.1016/j.cell.2017.07.023.
26. Piers, T.M., Cosker, K., Mallach, A., Johnson, G.T., Guerreiro, R., Hardy, J., and Pocock, J.M. (2020). A locked immunometabolic switch underlies TREM2 R47H loss of function in human iPSC-derived microglia. FASEB J. *34*, 2436–2450. https://doi.org/10.1096/fj.201902447R.
27. Keren-Shaul, H., Spinrad, A., Weiner, A., Matcovitch-Natan, O., Dvir-Szternfeld, R., Ulland, T.K., David, E., Baruch, K., Lara-Astaiso, D., Toth, B., et al. (2017). A unique microglia type associated with restricting development of Alzheimer's disease. Cell *169*, 1276–1290.e17. https://doi.org/10.1016/j.cell.2017.05.018.
28. Krasemann, S., Madore, C., Cialic, R., Baufeld, C., Calcagno, N., El Fatimy, R., Beckers, L., O'Loughlin, E., Xu, Y., Fanek, Z., et al. (2017). The TREM2-APOE pathway drives the transcriptional phenotype of dysfunctional microglia in neurodegenerative diseases.

Immunity *47*, 566–581.e9. https://doi.org/10.1016/j.immuni.2017.08.008.

29. Kleinberger, G., Brendel, M., Mracsko, E., Wefers, B., Groeneweg, L., Xiang, X., Focke, C., Deußing, M., Suárez-Calvet, M., Mazaheri, F., et al. (2017). The FTD-like syndrome causing TREM2 T66M mutation impairs microglia function, brain perfusion, and glucose metabolism. EMBO J. *36*, 1837–1853. https://doi.org/10.15252/EMBJ.201796516.

30. Götzl, J.K., Brendel, M., Werner, G., Parhizkar, S., Sebastian Monasor, L., Kleinberger, G., Colombo, A.-V., Deussing, M., Wagner, M., Winkelmann, J., et al. (2019). Opposite microglial activation stages upon loss of PGRN or TREM2 result in reduced cerebral glucose metabolism. EMBO Mol. Med. *11*, e9711. https://doi.org/10.15252/emmm.201809711.

31. Xiang, X., Wind, K., Wiedemann, T., Blume, T., Shi, Y., Briel, N., Beyer, L., Biechele, G., Eckenweber, F., Zatcepin, A., et al. (2021). Microglial activation states drive glucose uptake and FDG-PET alterations in neurodegenerative diseases. Sci. Transl. Med. *13*, eabe5640. https://doi.org/10.1126/scitranslmed.abe5640.

32. Cheng, Q., Danao, J., Talreja, S., Wen, P., Yin, J., Sun, N., Li, C.-M., Chui, D., Tran, D., Koirala, S., et al. (2018). TREM2-activating antibodies abrogate the negative pleiotropic effects of the Alzheimer's disease variant Trem2R47H on murine myeloid cell function. J. Biol. Chem. *293*, 12620–12633. https://doi.org/10.1074/jbc.RA118.001848.

33. Schlepckow, K., Monroe, K.M., Kleinberger, G., Cantuti-Castelvetri, L., Parhizkar, S., Xia, D., Willem, M., Werner, G., Pettkus, N., Brunner, B., et al. (2020). Enhancing protective microglial activities with a dual function TREM2 antibody to the stalk region. EMBO Mol. Med. *12*, e11227. https://doi.org/10.15252/emmm.201911227.

34. Wang, S., Mustafa, M., Yuede, C.M., Salazar, S.V., Kong, P., Long, H., Ward, M., Siddiqui, O., Paul, R., Gilfillan, S., et al. (2020). Anti-human TREM2 induces microglia proliferation and reduces pathology in an Alzheimer's disease model. J. Exp. Med. *217*, e20200785. https://doi.org/10.1084/jem.20200785.

35. Fassler, M., Rappaport, M.S., Cuño, C.B., and George, J. (2021). Engagement of TREM2 by a novel monoclonal antibody induces activation of microglia and improves cognitive function in Alzheimer's disease models. J. Neuroinflamm. *18*, 19. https://doi.org/10.1186/s12974-020-01980-5.

36. Okuzono, Y., Sakuma, H., Miyakawa, S., Ifuku, M., Lee, J., Das, D., Banerjee, A., Zhao, Y., Yamamoto, K., Ando, T., and Sato, S. (2021). Reduced TREM2 activation in microglia of patients with Alzheimer's disease. FEBS Open Bio *11*, 3063–3080. https://doi.org/10.1002/2211-5463.13300.

37. Pauls, S.D., and Marshall, A.J. (2017). Regulation of immune cell signaling by SHIP1: a phosphatase, scaffold protein, and potential therapeutic target. Eur. J. Immunol. *47*, 932–945. https://doi.org/10.1002/eji.201646795.

38. Balla, T. (2013). Phosphoinositides: tiny lipids with giant impact on cell regulation. Physiol. Rev. *93*, 1019–1137. https://doi.org/10.1152/physrev.00028.2012.

39. Robins, C., Liu, Y., Fan, W., Duong, D.M., Meigs, J., Harerimana, N.v., Gerasimov, E.S., Dammer, E.B., Cutler, D.J., Beach, T.G., et al. (2021). Genetic control of the human brain proteome. Am. J. Hum. Genet. *108*, 400–410. https://doi.org/10.1016/j.ajhg.2021.01.012.

40. Peng, Q., Malhotra, S., Torchia, J.A., Kerr, W.G., Coggeshall, K.M., and Humphrey, M.B. (2010). TREM2- and DAP12-dependent activation of PI3K requires DAP10 and is inhibited by SHIP1. Sci. Signal. *3*, ra38. https://doi.org/10.1126/scisignal.2000500.

41. Saito, T., Matsuba, Y., Mihira, N., Takano, J., Nilsson, P., Itohara, S., Iwata, N., and Saido, T.C. (2014). Single app knock-in mouse models of Alzheimer's disease. Nat. Neurosci. *17*, 661–663. https://doi.org/10.1038/nn.3697.

42. Tsai, A.P., Lin, P.B.-C., Dong, C., Moutinho, M., Casali, B.T., Liu, Y., Lamb, B.T., Landreth, G.E., Oblak, A.L., and Nho, K. (2021). INPP5D expression is associated with risk for Alzheimer's disease and induced by plaque-associated microglia. Neurobiol. Dis. *153*, 105303. https://doi.org/10.1016/j.nbd.2021.105303.

43. Helgason, C.D., Damen, J.E., Rosten, P., Grewal, R., Sorensen, P., Chappel, S.M., Borowski, A., Jirik, F., Krystal, G., and Humphries, R.K. (1998). Targeted disruption of SHIP leads to hemopoietic perturbations, lung pathology, and a shortened life span. Genes Dev. *12*, 1610–1620. https://doi.org/10.1101/gad.12.11.1610.

44. Zheng, H., Jia, L., Liu, C.-C., Rong, Z., Zhong, L., Yang, L., Chen, X.-F., Fryer, J.D., Wang, X., Zhang, Y.-W., et al. (2017). TREM2 promotes microglial survival by activating Wnt/β-catenin pathway. J. Neurosci. *37*, 1772–1784. https://doi.org/10.1523/JNEUROSCI.2459-16.2017.

45. Holtman, I.R., Skola, D., and Glass, C.K. (2017). Transcriptional control of microglia phenotypes in health and disease. J. Clin. Invest. *127*, 3220–3229. https://doi.org/10.1172/JCI90604.

46. Haure-Mirande, J.-V., Audrain, M., Fanutza, T., Kim, S.H., Klein, W.L., Glabe, C., Readhead, B., Dudley, J.T., Blitzer, R.D., Wang, M., et al. (2017). Deficiency of TYROBP, an adapter protein for TREM2 and CR3 receptors, is neuroprotective in a mouse model of early Alzheimer's pathology. Acta Neuropathol. *134*, 769–788. https://doi.org/10.1007/s00401-017-1737-3.

47. Escartin, C., Galea, E., Lakatos, A., O'Callaghan, J.P., Petzold, G.C., Serrano-Pozo, A., Steinhäuser, C., Volterra, A., Carmignoto, G., Agarwal, A., et al. (2021). Reactive astrocyte nomenclature, definitions, and future directions. Nat. Neurosci. *24*, 312–325. https://doi.org/10.1038/s41593-020-00783-4.

48. Liddelow, S.A., Guttenplan, K.A., Clarke, L.E., Bennett, F.C., Bohlen, C.J., Schirmer, L., Bennett, M.L., Münch, A.E., Chung, W.S., Peterson, T.C., et al. (2017). Neurotoxic reactive astrocytes are induced by activated microglia. Nature *541*, 481–487. https://doi.org/10.1038/nature21029.

49. Kidana, K., Tatebe, T., Ito, K., Hara, N., Kakita, A., Saito, T., Takatori, S., Ouchi, Y., Ikeuchi, T., Makino, M., et al. (2018). Loss of kallikrein-related peptidase 7 exacerbates amyloid pathology in Alzheimer's disease model mice. EMBO Mol. Med. *10*, e8184. https://doi.org/10.15252/emmm.201708184.

50. Masuda, A., Kobayashi, Y., Kogo, N., Saito, T., Saido, T.C., and Itohara, S. (2016). Cognitive deficits in single App knock-in mouse models. Neurobiol. Learn. Mem. *135*, 73–82. https://doi.org/10.1016/j.nlm.2016.07.001.

51. Jay, T.R., Hirsch, A.M., Broihier, M.L., Miller, C.M., Neilson, L.E., Ransohoff, R.M., Lamb, B.T., and Landreth, G.E. (2017). Disease progression-dependent effects of TREM2 deficiency in a mouse model of Alzheimer's disease. J. Neurosci. *37*, 637–647. https://doi.org/10.1523/JNEUROSCI.2110-16.2016.

52. Spangenberg, E., Severson, P.L., Hohsfield, L.A., Crapser, J., Zhang, J., Burton, E.A., Zhang, Y., Spevak, W., Lin, J., Phan, N.Y., et al. (2019). Sustained microglial depletion with CSF1R inhibitor impairs parenchymal plaque development in an Alzheimer's disease model. Nat. Commun. *10*, 3758. https://doi.org/10.1038/s41467-019-11674-z.

53. Ulrich, J.D., Ulland, T.K., Mahan, T.E., Nyström, S., Nilsson, K.P., Song, W.M., Zhou, Y., Reinartz, M., Choi, S., Jiang, H., et al. (2018). ApoE facilitates the microglial response to amyloid plaque pathology. J. Exp. Med. *215*, 1047–1058. https://doi.org/10.1084/JEM.20171265.

54. Parhizkar, S., Arzberger, T., Brendel, M., Kleinberger, G., Deussing, M., Focke, C., Nuscher, B., Xiong, M., Ghasemigharagoz, A., Katzmarski, N., et al. (2019). Loss of TREM2 function increases amyloid seeding but reduces plaque-associated ApoE. Nat. Neurosci. *22*, 191–204. https://doi.org/10.1038/S41593-018-0296-9.

55. Condello, C., Yuan, P., Schain, A., and Grutzendler, J. (2015). Microglia constitute a barrier that prevents neurotoxic protofibrillar Aβ42 hotspots around plaques. Nat. Commun. *6*, 6176. https://doi.org/10.1038/ncomms7176.

56. Zhao, J., Fu, Y., Yasvoina, M., Shao, P., Hitt, B., O'Connor, T., Logan, S., Maus, E., Citron, M., Berry, R., et al. (2007). Beta-site amyloid precursor protein cleaving enzyme 1 levels become elevated in neurons around amyloid plaques: implications for Alzheimer's disease pathogenesis. J. Neurosci. *27*, 3639–3649. https://doi.org/10.1523/JNEUROSCI.4396-06.2007.

57. Sharoar, M.G., Hu, X., Ma, X.-M., Zhu, X., and Yan, R. (2019). Sequential formation of different layers of dystrophic neurites in Alzheimer's brains. Mol. Psychiatry *24*, 1369–1382. https://doi.org/10.1038/s41380-019-0396-2.

58. Dickson, D.W., Wertkin, A., Mattiace, L.A., Fier, E., Kress, Y., Davies, P., and Yen, S.H. (1990). Ubiquitin immunoelectron microscopy of dystrophic neurites in cerebellar senile plaques of Alzheimer's disease. Acta Neuropathol. *79*, 486–493. https://doi.org/10.1007/BF00296107.

59. Su, W., Sun, J., Shimizu, K., and Kadota, K. (2019). TCC-GUI: a Shiny-based application for differential expression analysis of RNA-Seq count data. BMC Res. Notes *12*, 133. https://doi.org/10.1186/s13104-019-4179-2.

60. Griciuc, A., Patel, S., Federico, A.N., Choi, S.H., Innes, B.J., Oram, M.K., Cereghetti, G., McGinty, D., Anselmo, A., Sadreyev, R.I., et al. (2019). TREM2 acts downstream of CD33 in modulating microglial pathology in Alzheimer's disease. Neuron *103*, 820–835.e7. https://doi.org/10.1016/j.neuron.2019.06.010.

61. Haure-Mirande, J.-V., Wang, M., Audrain, M., Fanutza, T., Kim, S.H., Heja, S., Readhead, B., Dudley, J.T., Blitzer, R.D., Schadt, E.E., et al. (2019). Integrative approach to sporadic Alzheimer's disease: deficiency of TYROBP in cerebral Aβ amyloidosis mouse normalizes clinical phenotype and complement subnetwork molecular pathology without reducing Aβ burden. Mol. Psychiatry *24*, 431–446. https://doi.org/10.1038/s41380-018-0255-6.

62. Nugent, A.A., Lin, K., van Lengerich, B., Lianoglou, S., Przybyla, L., Davis, S.S., Llapashtica, C., Wang, J., Kim, D.J., Xia, D., et al. (2020). TREM2 regulates microglial cholesterol metabolism upon chronic phagocytic challenge. Neuron *105*, 837–854.e9. https://doi.org/10.1016/j.neuron.2019.12.007.

63. Karasawa, T., Yokokura, H., Kitajewski, J., and Lombroso, P.J. (2002). Frizzled-9 is activated by Wnt-2 and functions in Wnt/β-catenin signaling. J. Biol. Chem. *277*, 37479–37486. https://doi.org/10.1074/jbc.M205658200.

64. Wang, Y., Luo, W., Wang, X., Ma, Y., Huang, L., and Wang, Y. (2022). MAMDC2, a gene highly expressed in microglia in experimental models of Alzheimers Disease, positively regulates the innate antiviral response during neurotropic virus infection. J. Infect. *84*, 187–204. https://doi.org/10.1016/j.jinf.2021.12.004.

65. Kummer, M.P., Ising, C., Kummer, C., Sarlus, H., Griep, A., Vieira-Saecker, A., Schwartz, S., Halle, A., Brückner, M., Händler, K., et al. (2021). Microglial PD-1 stimulation by astrocytic PD-L1 suppresses neuroinflammation and Alzheimer's disease pathology. EMBO J. *40*, e108662. https://doi.org/10.15252/embj.2021108662.

66. Hu, Y.H., Zhang, Y., Jiang, L.Q., Wang, S., Lei, C.Q., Sun, M.S., Shu, H.B., and Liu, Y. (2015). WDFY1 mediates TLR3/4 signaling by recruiting TRIF. EMBO Rep. *16*, 447–455. https://doi.org/10.15252/embr.201439637.

67. Gabhann, J.N., Higgs, R., Brennan, K., Thomas, W., Damen, J.E., Ben Larbi, N., Krystal, G., and Jefferies, C.A. (2010). Absence of SHIP-1 results in constitutive phosphorylation of tank-binding kinase 1 and enhanced TLR3-dependent IFN-β production. J. Immunol. *184*, 2314–2320. https://doi.org/10.4049/jimmunol.0902589.

68. Bae, Y.S., Cantley, L.G., Chen, C.S., Kim, S.R., Kwon, K.S., and Rhee, S.G. (1998). Activation of phospholipase C-gamma by phosphatidylinositol 3,4,5-trisphosphate. J. Biol. Chem. *273*, 4465–4469. https://doi.org/10.1074/JBC.273.8.4465.

69. Falasca, M., Logan, S.K., Lehto, V.P., Baccante, G., Lemmon, M.A., and Schlessinger, J. (1998). Activation of phospholipase Cγ by PI 3-kinase-induced PH domain-mediated membrane targeting. EMBO J. *17*, 414–422. https://doi.org/10.1093/EMBOJ/17.2.414.

70. Gratacap, M.P., Payrastre, B., Viala, C., Mauco, G., Plantavid, M., and Chap, H. (1998). Phosphatidylinositol 3,4,5-trisphosphate-dependent stimulation of phospholipase C-gamma2 is an early key event in FcgammaRIIA-mediated activation of human platelets. J. Biol. Chem. *273*, 24314–24321. https://doi.org/10.1074/JBC.273.38.24314.

71. Watanabe, D., Hashimoto, S., Ishiai, M., Matsushita, M., Baba, Y., Kishimoto, T., Kurosaki, T., and Tsukada, S. (2001). Four tyrosine residues in phospholipase C-gamma 2, identified as Btk-dependent phosphorylation sites, are required for B cell antigen receptor-coupled calcium signaling. J. Biol. Chem. *276*, 38595–38601. https://doi.org/10.1074/JBC.M103675200.

72. Liu, S.-L., Wang, Z.-G., Hu, Y., Xin, Y., Singaram, I., Gorai, S., Zhou, X., Shim, Y., Min, J.-H., Gong, L.-W., et al. (2018). Quantitative lipid imaging reveals a new signaling function of phosphatidylinositol-3,4-bisphophate: isoform- and site-specific activation of Akt. Mol. Cell *71*, 1092–1104.e5. https://doi.org/10.1016/j.molcel.2018.07.035.

73. Söderberg, O., Gullberg, M., Jarvius, M., Ridderstråle, K., Leuchowius, K.J., Jarvius, J., Wester, K., Hydbring, P., Bahram, F., Larsson, L.G., and Landegren, U. (2006). Direct observation of individual endogenous protein complexes in situ by proximity ligation. Nat. Methods *3*, 995–1000. https://doi.org/10.1038/NMETH947.

74. Ong, C.J., Ming-Lum, A., Nodwell, M., Ghanipour, A., Yang, L., Williams, D.E., Kim, J., Demirjian, L., Qasimi, P., Ruschmann, J., et al. (2007). Small-molecule agonists of SHIP1 inhibit the phosphoinositide 3-kinase pathway in hematopoietic cells. Blood *110*, 1942–1949. https://doi.org/10.1182/blood-2007-03-079699.

75. Malik, M., Parikh, I., Vasquez, J.B., Smith, C., Tai, L., Bu, G., LaDu, M.J., Fardo, D.W., Rebeck, G.W., and Estus, S. (2015). Genetics ignite focus on microglial inflammation in Alzheimer's disease. Mol. Neurodegener. *10*, 52. https://doi.org/10.1186/s13024-015-0048-1.

76. Karahan, H., Smith, D.C., Kim, B., Dabin, L.C., Al-Amin, M.M., Wijeratne, H.R.S., Pennington, T., Viana di Prisco, G., McCord, B., Lin, P.B.C., et al. (2021). Deletion of Abi3 gene locus exacerbates neuropathological features of Alzheimer's disease in a mouse model of Aβ amyloidosis. Sci. Adv. *7*, eabe3954. https://doi.org/10.1126/SCIADV.ABE3954.

77. Mazaheri, F., Snaidero, N., Kleinberger, G., Madore, C., Daria, A., Werner, G., Krasemann, S., Capell, A., Trümbach, D., Wurst, W., et al. (2017). TREM2 deficiency impairs chemotaxis and microglial responses to neuronal injury. EMBO Rep. *18*, 1186–1198. https://doi.org/10.15252/embr.201743922.

78. McQuade, A., Kang, Y.J., Hasselmann, J., Jairaman, A., Sotelo, A., Coburn, M., Shabestari, S.K., Chadarevian, J.P., Fote, G., Tu, C.H., et al. (2020). Gene expression and functional deficits underlie TREM2-knockout microglia responses in human models of Alzheimer's disease. Nat. Commun. *11*, 5370. https://doi.org/10.1038/s41467-020-19227-5.

79. Castranio, E.L., Hasel, P., Haure-Mirande, J., Ramirez Jimenez, A.v., Hamilton, B.W., Kim, R.D., Glabe, C.G., Wang, M., Zhang, B., Gandy, S., et al. (2022). Microglial INPP5D limits plaque formation and glial reactivity in the PSAPP mouse model of Alzheimer's disease. Alzheimer's Dement. https://doi.org/10.1002/ALZ.12821.

80. Lin, P.B., Tsai, A.P., Soni, D., Lee-Gosselin, A., Moutinho, M., Puntambekar, S.S., Landreth, G.E., Lamb, B.T., and Oblak, A.L. (2022). INPP5D deficiency attenuates amyloid pathology in a mouse model of Alzheimer's disease. Alzheimer's Dement. https://doi.org/10.1002/ALZ.12849.

81. Grathwohl, S.A., Kälin, R.E., Bolmont, T., Prokop, S., Winkelmann, G., Kaeser, S.A., Odenthal, J., Radde, R., Eldh, T., Gandy, S., et al. (2009). Formation and maintenance of Alzheimer's disease beta-amyloid plaques in the absence of microglia. Nat. Neurosci. *12*, 1361–1363. https://doi.org/10.1038/NN.2432.

82. Sadleir, K.R., Kandalepas, P.C., Buggia-Prévot, V., Nicholson, D.A., Thinakaran, G., and Vassar, R. (2016). Presynaptic dystrophic neurites surrounding amyloid plaques are sites of microtubule disruption, BACE1 elevation, and increased Aβ generation in Alzheimer's disease. Acta Neuropathol. *132*, 235–256. https://doi.org/10.1007/s00401-016-1558-9.

83. Jay, T.R., Miller, C.M., Cheng, P.J., Graham, L.C., Bemiller, S., Broihier, M.L., Xu, G., Margevicius, D., Karlo, J.C., Sousa, G.L., et al. (2015). TREM2 deficiency eliminates TREM2+ inflammatory macrophages and ameliorates pathology in Alzheimer's disease mouse models. J. Exp. Med. *212*, 287–295. https://doi.org/10.1084/jem.20142322.

84. Chatterjee, P., Pedrini, S., Stoops, E., Goozee, K., Villemagne, V.L., Asih, P.R., Verberk, I.M.W., Dave, P., Taddei, K., Sohrabi, H.R., et al. (2021). Plasma glial fibrillary acidic protein is elevated in cognitively normal older adults at risk of Alzheimer's disease. Transl. Psychiatry *11*, 27. https://doi.org/10.1038/s41398-020-01137-1.

85. Benedet, A.L., Milà-Alomà, M., Vrillon, A., Ashton, N.J., Pascoal, T.A., Lussier, F., Karikari, T.K., Hourregue, C., Cognat, E., Dumurgier, J., et al. (2021). Differences

between plasma and cerebrospinal fluid glial fibrillary acidic protein levels across the Alzheimer disease continuum. JAMA Neurol. *78*, 1471–1483. https://doi.org/10.1001/jamaneurol.2021.3671.

86. Takahashi, K., Rochford, C.D.P., and Neumann, H. (2005). Clearance of apoptotic neurons without inflammation by microglial triggering receptor expressed on myeloid cells-2. J. Exp. Med. *201*, 647–657. https://doi.org/10.1084/jem.20041611.

87. Hall-Roberts, H., Agarwal, D., Obst, J., Smith, T.B., Monzón-Sandoval, J., Di Daniel, E., Webber, C., James, W.S., Mead, E., Davis, J.B., and Cowley, S.A. (2020). TREM2 Alzheimer's variant R47H causes similar transcriptional dysregulation to knockout, yet only subtle functional phenotypes in human iPSC-derived macrophages. Alzheimer's Res. Ther. *12*, 151. https://doi.org/10.1186/s13195-020-00709-z.

88. Koenigsknecht, J., and Landreth, G. (2004). Microglial phagocytosis of fibrillar beta-amyloid through a beta1 integrin-dependent mechanism. J. Neurosci. *24*, 9838–9846. https://doi.org/10.1523/JNEUROSCI.2557-04.2004.

89. Huang, Y., Happonen, K.E., Burrola, P.G., O'Connor, C., Hah, N., Huang, L., Nimmerjahn, A., and Lemke, G. (2021). Microglia use TAM receptors to detect and engulf amyloid β plaques. Nat. Immunol. *22*, 586–594. https://doi.org/10.1038/s41590-021-00913-5.

90. Ennerfelt, H., Frost, E.L., Shapiro, D.A., Holliday, C., Zengeler, K.E., Voithofer, G., Bolte, A.C., Lammert, C.R., Kulas, J.A., Ulland, T.K., and Lukens, J.R. (2022). SYK coordinates neuroprotective microglial responses in neurodegenerative disease. Cell *185*, 4135–4152.e22. https://doi.org/10.1016/J.CELL.2022.09.030.

91. Wang, S., Sudan, R., Peng, V., Zhou, Y., Du, S., Yuede, C.M., Lei, T., Hou, J., Cai, Z., Cella, M., et al. (2022). TREM2 drives microglia response to amyloid-β via SYK-dependent and -independent pathways. Cell *185*, 4153–4169.e19. https://doi.org/10.1016/J.CELL.2022.09.033.

92. Deming, Y., Li, Z., Kapoor, M., Harari, O., Del-Aguila, J.L., Black, K., Carrell, D., Cai, Y., Fernandez, M.V., Budde, J., et al. (2017). Genome-wide association study identifies four novel loci associated with Alzheimer's endophenotypes and disease modifiers. Acta Neuropathol. *133*, 839–856. https://doi.org/10.1007/s00401-017-1685-y.

93. Yao, X., Risacher, S.L., Nho, K., Saykin, A.J., Wang, Z., and Shen, L.; Alzheimer's Disease Neuroimaging Initiative (2019). Targeted genetic analysis of cerebral blood flow imaging phenotypes implicates the INPP5D gene. Neurobiol. Aging *81*, 213–221. https://doi.org/10.1016/j.neurobiolaging.2019.06.003.

94. Tan, M.-S., Yang, Y.-X., Xu, W., Wang, H.-F., Tan, L., Zuo, C.-T., Dong, Q., Tan, L., Suckling, J., and Yu, J.-T.; Alzheimer's Disease Neuroimaging Initiative (2021). Associations of Alzheimer's disease risk variants with gene expression, amyloidosis, tauopathy, and neurodegeneration. Alzheimer's Res. Ther. *13*, 15. https://doi.org/10.1186/s13195-020-00755-7.

95. Nishio, M., Watanabe, K.i., Sasaki, J., Taya, C., Takasuga, S., Iizuka, R., Balla, T., Yamazaki, M., Watanabe, H., Itoh, R., et al. (2007). Control of cell polarity and motility by the PtdIns(3,4,5)P3 phosphatase SHIP1. Nat. Cell Biol. *9*, 36–44. https://doi.org/10.1038/ncb1515.

96. Kaifu, T., Nakahara, J., Inui, M., Mishima, K., Momiyama, T., Kaji, M., Sugahara, A., Koito, H., Ujike-Asai, A., Nakamura, A., et al. (2003). Osteopetrosis and thalamic hypomyelinosis with synaptic degeneration in DAP12-deficient mice. J. Clin. Invest. *111*, 323–332. https://doi.org/10.1172/JCI16923.

97. Takenouchi, T., Ogihara, K., Sato, M., and Kitani, H. (2005). Inhibitory effects of U73122 and U73343 on Ca2+ influx and pore formation induced by the activation of P2X7 nucleotide receptors in mouse microglial cell line. Biochim. Biophys. Acta *1726*, 177–186. https://doi.org/10.1016/J.BBAGEN.2005.08.001.

98. Nakamichi, K., Saiki, M., Kitani, H., Kuboyama, Y., Morimoto, K., Takayama-Ito, M., and Kurane, I. (2006). Suppressive effect of simvastatin on interferon-beta-induced expression of CC chemokine ligand 5 in microglia. Neurosci. Lett. *407*, 205–210. https://doi.org/10.1016/J.NEULET.2006.08.044.

STAR★METHODS

KEY RESOURCES TABLE

REAGENT or RESOURCE	SOURCE	IDENTIFIER
Antibodies		
Rabbit polyclonal anti-Iba1	FUJIFILM Wako	Cat# 019-19741, RRID: AB_839504
Goat polyclonal anti-Iba1	FUJIFILM Wako	Cat# 011-27991
Mouse monoclonal anti-Human Amyloid-beta (N) (82E1)	Immuno-Biological Laboratories	Cat# JP10323, RRID:AB_163080
Rabbit monoclonalanti-β-Amyloid (D54D2)	Cell Signaling Technology	Cat# 8243, RRID: AB_279764
Mouse monoclonal anti-β-Amyloid (6E10)	Covance	Cat# SIG-39320, RRID: AB_662798
Rabbit monoclonalanti-PU.1 (9G7)	Cell Signaling Technology	Cat# 2258, RRID: AB_218690
Rabbit monoclonal anti-BACE (D10E5)	Cell Signaling Technology	Cat# 5606, RRID: AB_190390
Chicken polyclonal anti-GFAP	BioLegend	Cat# 829401, RRID: AB_256492
Goat polyclonal anti-Apolipoprotein E	Merck/Millipore	Cat# AB947, RRID: AB_2258475
Rabbit monoclonal anti-Phospho-Akt (Ser473) (D9E)	Cell Signaling Technology	Cat# 4060, RRID: AB_231504
Rabbit monoclonal anti-Akt (pan) (C67E7)	Cell Signaling Technology	Cat# 4691, RRID: AB_915783
Rabbit polyclonal anti-PLC-gamma-2	Cell Signaling Technology	Cat# 3872, RRID: AB_229958
Rabbit polyclonal anti-Phospho-PLC-gamma-2 (Tyr1217)	Cell Signaling Technology	Cat# 3871, RRID: AB_229954
Mouse monoclonal anti-Phospho-Erk (E-4)	Santa Cruz Biotechnology	Cat# sc-7383, RRID: AB_627545
Rabbit monoclonal anti-p44/42 MAPK (Erk1/2) (137F5)	Cell Signaling Technology	Cat# 4695, RRID: AB_390779
Mouse monoclonal anti-LC3B (E5Q2K)	Cell Signaling Technology	Cat# 83506, RRID: AB_2800018
Rabbit monoclonalanti-TREM2 (E7P8J)	Cell Signaling Technology	Cat# 76765, RRID: AB_279988
Rabbit monoclonalanti-DAP12 (D7G1X)	Cell Signaling Technology	Cat# 12492, RRID: AB_272112
Mouse monoclonal anti-SYK (SYK-01)	BioLegend	Cat# 626202RRID: AB_2200268
Rabbit monoclonalanti-PTEN (138G6)	Cell Signaling Technology	Cat# 9559, RRID: AB_390810
Mouse monoclonal anti-SHIP1 (P1C1)	Santa Cruz Biotechnology	Cat# sc-8425, RRID: AB_628250
Rabbit monoclonal anti-Inpp4a (EP3425(2))	abcam	Cat# ab109622, RRID: AB_10887220
Rabbit monoclonal anti-Inppl1 (EPR10955)	abcam	Cat# ab166916, RRID: AB_268689
Mouse monoclonalanti-α-Tubulin (clone DM1A)	Sigma-Aldrich	Cat# T9026, RRID: AB_477593
Rabbit polyclonal anti-Ubiquitin	Dako	Cat# Z0458, RRID: AB_231552
Rabbit monoclonal anti-Phospho-tau (EPR20390)	abcam	Cat# ab210703, RRID: AB_2922760
Mouse monoclonal anti-Phospho-tau (Ser202, Thr205) (Clone AT8)	Thermo Fisher	Cat# MN1020, RRID: AB_223647
Rabbit monoclonal anti-Tmem119 (28-3)	abcam	Cat# 209064, RRID: AB_272808
Armenian Hamster monoclonal anti-mouse CD11c (Clone ID N418)	BioLegend	Cat# 117301, RRID: AB_313770
Rabbit polyclonal anti-P2RY12 antibody	Sigma-Aldrich	Cat# HPA013796, RRID: AB_1854884
Mouse monoclonal anti-DYKDDDDK tag (Clone 1E6)	FUJIFILM Wako	Cat# 012-22384, RRID: AB_10659717
Rabbit polyclonal anti-DYKDDDDK tag	Cell Signaling Technology	Cat# 2368, RRID: AB_2217020
Rabbit polyclonal anti-V5 tag	MBL	Cat# PM003, RRID: AB_592941
Rat monoclonal anti-mouse/human CD11b FITC	BioLegend	Cat# 101205, RRID: AB_312788
Mouse monoclonal anti-SHIP-1 (Clone P1C1-A5) PE	BioLegend	Cat# 656604, RRID: AB_256286
Rat monoclonal anti-mouse CD45 Alexa Fluor® 647	BioLegend	Cat# 103124, RRID: AB_493533
Rat monoclonal anti-mouse CD16/32	BioLegend	Cat# 101302, RRID: AB_312801
Goat Anti-Rabbit Peroxidase	Jackson ImmunoResearch	Cat# 111-035-144, RRID: AB_2307391
Goat Anti-Mouse Peroxidase	Jackson ImmunoResearch	Cat# 115-035-003, RRID: AB_10015289

(*Continued on next page*)

Continued

REAGENT or RESOURCE	SOURCE	IDENTIFIER
Horse Anti-Mouse IgG Antibody (H+L), Biotinylated	Vector Laboratories	Cat# BA-2000, RRID: AB_2313581
Rabbit Anti-Goat IgG Antibody (H+L), Biotinylated	Vector Laboratories	Cat# BA-5000, RRID: AB_2336126
Normal mouse IgG, whole molecule, purified	FUJIFILM Wako	Cat# 140-09511
Mouse TREM2 Antibody	R&D Systems	Cat# AF1729, RRID: AB_354956
Normal Sheep IgG Control	R&D Systems	Cat# 5-001-A, RRID: AB_10141430
Chemicals, peptides, and recombinant proteins		
10×HBSS(−) without Phenol Red	FUJIFILM Wako	Cat# 082-09865
Percoll Plus	GE Healthcare	Cat# 17544502
HBSS(−) without Phenol Red	FUJIFILM Wako	Cat# 085-09355
Lipofectamine™ RNAiMAX Transfection Reagent	Thermo Fisher	Cat# 13778500
Thioflavin S, practical grade	SIGMA	Cat# T1892-25G
Sudan Black B	Merck	Cat# 1.15928.0025
Propidium iodide	Sigma-Aldrich	Cat# P4170
Paraformaldehyde	FUJIFILM Wako	Cat# 162-16065
Albumin, from Bovine Serum, Fraction V pH7.0	FUJIFILM Wako	Cat# 013-27054
Lipopolysaccharides from *Escherichia coli* O111:B4	Sigma-Aldrich	Cat# L4391
Cholera Toxin Subunit B (Recombinant), Alexa Fluor 647 Conjugate	Thermo Fisher	Cat# C34778
Recombinant Mouse Complement Component C5a Protein	R&D Systems	Cat# 2150-C5-025
ProLong Diamond Antifade Mountant with DAPI	Thermo Fisher	Cat# P36962
Protein G Sepharose 4 Fast Flow	Cytiva	Cat# 17061801
Critical commercial assays		
Human β Amyloid(1-40) ELISA Kit Wako II	FUJIFILM Wako	Cat# 292-64601
Human/Rat β Amyloid(42) ELISA Kit Wako, High Sensitive	FUJIFILM Wako	Cat# 292-64501
Simoa NF-light Advantage Kit	Quanterix	Cat# 103186
Simoa NF-light Sample Diluent Reagent	Quanterix	Cat# 102252
ReverTra Ace® qPCR RT Master Mix with gDNA Remover	TOYOBO CO., LTD	Cat# FSQ-301
THUNDERBIRD® SYBR qPCR Mix	TOYOBO CO., LTD	Cat# QPS-201
RNeasy Plus Micro Kit	QIAGEN	Cat# 74034
TSA Plus Fluorescein 50-150 slides	AKOYA Biosciences	Cat# NEL741001KT
TSA Plus TMR 50-150 slides	AKOYA Biosciences	Cat# NEL742001KT
TSA Plus Cyanine 5 50-150 slides	AKOYA Biosciences	Cat# NEL745001KT
TSA Blocking Reagent	AKOYA Biosciences	Cat# FP1020
Proteinase K	TaKaRa	Cat# 9034
BCA Protein Assay Kit	TaKaRa	Cat# T9300A
Amicon Ultra 0.5 mL	Merck/Millipore	Cat# UFC505024
Cell culture insert, transparent PET membrane, 24-well, 8.0 μm pore size	Corning	Cat# 353097
alamarBlue®	Bio-Rad	Cat# BUF012A
Duolink® *In Situ* Detection Reagents Green	Sigma-Aldrich	Cat# DUO92014-30RXN
Duolink® *In Situ* PLA® Probe Anti-Mouse PLUS	Sigma-Aldrich	Cat# DUO92001, RRID: AB_2810939
Duolink® *In Situ* PLA® Probe Anti-Rabbit MINUS	Sigma-Aldrich	Cat# DUO92005, RRID: AB_2810942
Peroxidase Labeling Kit - NH2	Dojindo	Cat# LK11
Titansphere Phos-TiO2 Kit	GL Sciences	Cat# 5010-21305
GL-Tip SDB	GL Sciences	Cat# 7820-11200

(*Continued on next page*)

Continued

REAGENT or RESOURCE	SOURCE	IDENTIFIER
Deposited data		
Raw files of RNA-seq analysis	This study	NCBI-GEO:GSE172499
LC-MS/MS analysis of phosphopeptides isolated from primary microglia	This study	PXID: PXD040217 (jPOST: JPST002047)
Experimental models: Cell lines		
MG6	RIKEN BioResource Research Center	RRID:CVCL_8732
1D4B (Frozen Cells)	Developmental Studies Hybridoma Bank	Cat# 1D4B-f, RRID: AB_528127
Experimental models: Organisms/strains		
App(NL-G-F/NL-G-F)	Saito et al.[41]	IMSR Cat# RBRC06344, RRID:IMSR_RBRC06344
Inpp5d(+/−)	Nishio et al.[95]	N/A
Tyrobp(−/−)	Kaifu et al.[96]	N/A
Oligonucleotides		
qRT-PCR primers, see Table S1		N/A
siRNAs, see Table S1		N/A
Software and algorithms		
GraphPad Prism 8	GraphPad Software	RRID: SCR_002798
Imaris	Oxford Instruments	RRID: SCR_007370
Fiji (1.53c)	ImageJ	RRID: SCR_003070
RStudio (Version 1.3.1056)	RStudio, PBC	RRID: SCR_000432
R (Version 4.0.2)	R Foundation for Statistical Computing	RRID: SCR_001905
Proteome Discoverer (version 2.2.0.388)	Thermo Fisher	RRID: SCR_014477

RESOURCE AVAILABILITY

Lead contact

Further information and requests for resources and reagents should be directed to and will be fulfilled by the lead contact, Taisuke Tomita (taisuke@mol.f.u-tokyo.ac.jp).

Materials availability

Plasmids generated in this study will be available upon request.

Data and code availability

RNA-seq and proteomics data have been deposited at NCBI GEO and jPOSTrepo, respectively, and are publicly available as of the date of publication. Accession numbers are listed in the key resources table. All the data reported in this paper will be shared by the lead contact upon request.

This paper does not report original code.

Any additional information required to reanalyze the data reported in this paper is available from the lead contact upon request.

EXPERIMENTAL MODEL AND SUBJECT DETAILS

Mice

NLGF (IMSR Cat# RBRC06344, RRID:IMSR_RBRC06344),[41] *Inpp5d*$^{+/-}$[95] and *Tyrobp*$^{-/-}$[96] mice were described previously. All animal experiments were performed according to the protocols approved by the Institutional Animal Care Committee of the Graduate School of Pharmaceutical Sciences at the University of Tokyo (protocol no. P27-6, P2-2). All mice were housed under standard conditions (12-hour light and 12-hour dark cycle, 22°C, 40 to 60% of humidity) with free access to food and water. We used male mice except for the experiments in Figures 5 and S6C, in which female mice were used. We did not mix male and female mice in individual analyses (except for primary cell preparation) to avoid possible sex-dependent variations.

Primary microglia culture

Primary microglia were prepared from 3-day-old C57BL/6J male and female mice. After removing meninges, brains were incubated in Hank's balanced salt solution (HBSS) containing trypsin, deoxyribonuclease I, $CaCl_2$, $MgSO_4$ at 37°C for 20 min, gently triturating with a fine pipet tip every 5 min. Cells were added with DMEM supplemented with 10% FBS and penicillin/streptomycin (DMEM(+/+)) to quench the reaction and passed through a 100-μm strainer. Cells were spun at 300 g and room temperature for 10 min, resuspended in DMEM(+/+) and plated in T-75 flasks at the density of one brain per flask. At 4, 7 and 10 days *in vitro* (DIV), the medium was replaced with a fresh one. At 15 DIV, microglia were isolated by shaking flasks by hand for 1 min and centrifuged at 2,000 rpm and room temperature for 5 min. Cells were resuspended in medium supplemented with 10% L929-cell-conditioned medium (10% LCM) and cultured until use. The purity of isolated microglia was higher than 90% based on the flow cytometric analysis of the $CD11b^+$ cell population.

METHOD DETAILS

Brain sample collection and preparation

Mice were deeply anesthetized and perfused transcardially with 15 mL ice-cold phosphate-buffered saline (PBS). The brains were quickly removed and dissected into two hemispheres. The left hemispheres (for biochemical analyses) were flash-frozen in liquid nitrogen and stored at −80°C until use. The right hemispheres (for immunohistochemistry) were fixed in 4% paraformaldehyde (PFA) for 24 h at 4°C, followed by three washes and a cryoprotection with 30% sucrose, 0.02% NaN_3 in PBS. The brains were quickly frozen on dry ice and cut into 30-μm-thick coronal sections by using a sliding microtome.

Histochemistry on free-floating brain sections

Free-floating brain sections were blocked and permeabilized with 10% donkey serum, 0.1% Triton X-100 and 0.02% NaN_3 in PBS for 1 h at room temperature. If needed, antigen retrieval at 95°C for 10 min was performed before blocking. After 3 washes with PBS, brain sections were incubated with primary antibodies diluted in PBS overnight at 4°C. After 3 washes with PBS, sections were treated with secondary antibodies diluted in PBS for 2 h at room temperature. After 3 washes with PBS, the sections were mounted with ProLong Diamond Antifade Mountant with DAPI.

For the staining of PU.1, CD11c, and p-tau, TSA plus amplification kit (Perkin Elmer) was used in combination with subsequent conventional immunofluorescence staining for other antigens. To block endogenous peroxidase activity, brain sections were treated with 30% H_2O_2 in PBS for 15 min at room temperature. After washing, sections were treated with TNB buffer (100 mM Tris-HCl (pH 7.5), 150 mM NaCl containing 0.5% blocking reagent from Perkin Elmer) for 1 h at room temperature, and then incubated with primary antibody in TNB buffer overnight at 4°C. The sections were incubated with appropriate peroxidase-conjugated secondary antibodies diluted in TNB buffer at 4°C overnight. For CD11c staining, goat anti-Armenian hamster antibody (Jackson Immunoresearch) was used after conjugation with peroxidase using a commercial kit (LK-11, Dojindo). After 3 washes with TNT buffer (0.1% Triton X-100, 100 mM Tris-HCl (pH 7.5), 150 mM NaCl), the sections were reacted with TMR-amplification reagent for 10 min at room temperature, washed with TNT.

Thioflavin S staining was performed as below. To reduce autofluorescence, brain sections were treated with 0.1% Triton X-100 in PBS for 30 min and then incubated with 0.1% Sudan Black in 70% EtOH for 15 min. After 2 washes with 50% EtOH, sections were stained with 0.1% Thioflavin S in 20% EtOH for 15 min at room temperature, followed by 2 washes with 50% EtOH, 3 washes with 0.1% Triton X-100 in PBS, and final mounting with ProLong Diamond Antifade Mountant. If needed, this method was performed posterior to the immunofluorescence method as described above.

Immunohistochemistry on paraffin-embedded sections

For the longitudinal analysis of p-tau and BACE1 accumulation in Figure 5, paraffin-embedded brain sections from female *NLGF* mice were used, and the signals were amplified using TSA plus amplification kits. Deparaffinized sections were autoclaved at 121°C for 5 min in 10 mM Citrate-HCl (pH 6.0). After inactivation of endogenous peroxidases using 0.3% H_2O_2 in methanol for 30 min, the sections were blocked for 30 min in TNB buffer, and incubated with anti-phosphorylated tau (AT8) at 4°C overnight. On the second day, the sections were sequentially incubated with biotinylated anti-mouse and peroxidase-conjugated streptavidin, and then reacted with fluorescein-tyramide reagent for 10 min. After quenching the peroxidase activity using 0.3% H_2O_2, 0.1% NaN_3 in PBS, the sections were blocked and incubated with anti-BACE1 (D10E5) at 4°C overnight. On the third day, the sections were incubated with peroxidase-conjugated anti-rabbit for 1 h, and then reacted with tetramethylrhodamine-tyramide reagent for 10 min. The sections were subjected to microwave processing to remove antibodies, followed by peroxidase inactivation using 0.3% H_2O_2 in methanol. The sections were blocked and incubated with anti-Aβ (D54D2) at 4°C overnight. On the fourth day, the signal was amplified in the same way as BACE1, except for using Cy5-tyramide. Finally, the sections were mounted with ProLong Diamond Antifade Mountant with DAPI.

For ApoE staining, paraffin-embedded brain sections from 11 to 12 m.o. male mice were used. Deparaffinized sections were subjected to antigen retrieval by microwave heating (500 W for 10 min and then 100–200 W for 10 min in 10 mM Citrate-HCl, pH 6.0) followed by proteinase K treatment (TaKaRa; Dilution: 1/200 (v/v)) at 37°C for 7 min. After inactivation of endogenous peroxidase and blocking, sections were incubated with Goat anti-ApoE antibody (AB947) at 4°C overnight. The sections were treated with HRP-conjugated anti-Goat antibody (BA5000) for 1 h and then visualized using fluorescein-tyramide reagent as above.

Brain Aβ measurement by ELISA

Frozen brain hemispheres were mechanically homogenized with 30 strokes of Potter-Elvehjem tissue grinder for cortex or with 20 strokes of BioMasher II for hippocampus in 10 volumes of ice-cold Tris-buffered saline (pH 7.6) with protease/phosphatase inhibitors (TBS). After ultracentrifugation at 312,000 g and 4°C for 20 min, the supernatant was collected as the TBS-soluble fraction. The pellet was similarly extracted with 10 volumes of ice-cold 2% (v/v) Triton X-100 in TBS and then with room temperature 2% (w/v) SDS in TBS, each followed by ultracentrifugation yielding the supernatants referred to as the TX-soluble and the SDS-soluble fraction, respectively. The final pellet was re-solubilized in 70% formic acid (FA), clarified by ultracentrifugation at 312,000 g and 4°C for 20 min. The supernatant was neutralized by adding with neutralization buffer (1 M Tris, 0.5 M Na_2HPO_4, 0.05% NaN_3) and referred to as the FA-soluble fraction. The abundance of Aβ40 or Aβ42 in each fraction was measured by ELISA according to the manufacturer's instruction.

Isolation of microglia from adult mouse brain

Microglia were isolated from 9-month-old mouse brain by using fluorescence activated cell sorting (FACS). After perfusion with 15-mL HBSS, mice were quickly decapitated, and the brains were cut into two hemispheres. Only the left hemispheres were used for isolating cells, while the remaining hemispheres were kept for histochemical analyses. The left hemispheres were gently homogenized in HBSS using the Dounce homogenizer. Homogenates were centrifuged at 300 g and 4°C for 5 min, resuspended in 6 mL of 37% isotonic Percoll plus (#17544502, GE Healthcare), and underlaid with 6 mL of 70% isotonic Percoll solution. After centrifugation at 800*g* and room temperature for 30 min with no acceleration and no brake, the top layer (myelin debris) was discarded and 2 mL of the 37–70% interphase was collected. Cells were diluted with ice-cold HBSS and centrifuged at 300 g and 4°C for 5 min. Cells resuspended in FACS buffer (0.5% BSA, 2 mM EDTA, and 0.1% NaN_3 in Dulbecco's PBS(−)) were reacted with Fc blocker (BioLegend, #101302, 1:100) for 15 min on ice and then with anti-CD11b-FITC (BioLegend, #101206, 1:300), anti-CD45-Alexa 647 (BioLegend, #103124, 1:300) and propidium iodide (PI for dead cells, Sigma-Aldrich, #P4170, final concentration 100 ng/mL) for 20 min on ice in the dark. Cells were added with 5 mL of FACS buffer and spun at 300 g and 4°C for 5 min. Cells were resuspended in 500 μL of FACS buffer and passed through a filter-top tube (BD Falcon). $CD11b^+$ $CD45^+$ PI^- cells were sorted using BD FACSAria III Cell Sorter (BD Biosciences). Sorted cells were spun at 5,000 g and 4°C for 10 min, flash-frozen in liquid nitrogen and stored at −80°C until RNA extraction.

For quantitation of INPP5D by flow cytometry, isolated microglia were fixed with 4% PFA in PBS at room temperature for 15 min, washed with ice-cold PBS and permeabilized with ice-cold 90% methanol on ice for at least 20 min. After 2 washes with PBS, cells were treated with Fc blocker in FACS buffer on ice, and then added with anti-CD11b-FITC, anti-CD45-Alexa 647 and anti-SHIP-1-PE (INPP5D, BioLegend, #656604, 1:100) and incubated for 20 min on ice in the dark. INPP5D expression was measured in CD11b$^+$ CD45$^+$ cells.

Sample preparation for immunoblotting

Frozen brain hemispheres were mechanically homogenized with 30 strokes of Potter-Elvehjem tissue grinder in 10 volumes of ice-cold RIPA buffer with protease/phosphatase inhibitors. The homogenates were ultracentrifuged at 312,000 g and 4°C for 20 min. The supernatant was collected as a RIPA-soluble fraction and stored at −80°C until use. The pellet was re-solubilized in 70% formic acid, clarified by ultracentrifugation at 312,000 g and 4°C for 20 min, dried, solubilized in DMSO and used as a RIPA-insoluble, formic-acid-soluble fraction.

For MG6 and primary microglial cells, cells rinsed with ice-cold PBS were lysed/sonicated in a RIPA buffer containing protease/phosphatase inhibitors.

The protein concentration of the samples was measured by Bicinchoninic Acid Protein Assay (TaKaRa). 5× SDS-PAGE sample buffer and 2-mercaptoethanol to a final concentration of 1% (v/v) were added, and the samples were heated for 10 min at 100°C.

Immunoblotting

Proteins separated by Tris-Glycine or Tris-Tricine SDS polyacrylamide gel electrophoresis were transferred to PVDF membranes. The membranes were blocked for 1 h at room temperature with 5% skim milk or 3% BSA (for phospho-specific antibodies) in 0.1% (v/v) Tween 20 in TBS (TBST), followed by 3 washes with TBST. Membranes were incubated with appropriate dilutions of primary antibody in TBST with NaN_3 overnight at 4°C. After three washes with TBST, membranes were incubated with the appropriate peroxidase-conjugated secondary antibody (1:4,000) in TBST for 1 h at room temperature. After three washes with TBST, membranes were incubated with immunostar luminescence working solution. Signals were detected by ImageQuant LAS 4000 and processed using Image J/Fiji (1.53c).

Transfection of primary microglia

For transfection of small interfering RNA (siRNA; listed in Table S1), primary microglia were plated in a low-cell-binding 12-well plate at the density of 1.5×10^5 cells/well with 10% LCM. After two days, cells were transfected with siRNA using Lipofectamine RNAiMAX according to the manufacturer's instruction. After 24 h, the medium was replaced with a fresh one. Cells cultured for further 48 h were used for subsequent analyses.

Phosphoproteomic analysis of primary microglia

Primary microglia transfected with indicated siRNAs were lysed in SDS lysis buffer (4% SDS, 10 mM Tris pH 8.0), and proteins were precipitated using ice-cold acetone and resuspended in a buffer (10% 2-2-2-trifluorethanol, 100 mM ammonium bicarbonate). Proteins were reduced by tris(2-carboxyethyl)phosphine, S-alkylated with methyl methanethiosulfonate, and digested by LysC and trypsin overnight. Phosphopeptides were enriched using Titansphere Phos-TiO2 Kit and the eluates were desalted using GL-Tip SDB (GL Sciences) and dried under reduced pressure. The dried peptides were dissolved in a solvent (water: formic acid = 99.9: 0.1 by volume). Six microliter samples were subjected to EASY-nLC 1200 (Thermo Fisher Scientific) equipped with a 3-μm C18 nano HPLC capillary column (Nikkyo Technos, Cat#75-3-12), and separation was performed using mobile phase composed of solvent A (water/formic acid 100:0.1 (v:v)) and solvent B (water/acetonitrile/formic acid 5:95:0.1 (v:v:v)) at a constant flow rate of 300 nL/min, with the following conditions: an isocratic elution with 0% B for 5 min; a linear gradient of 10–40% B over the next 85 min; 40–95% B for 2 min; 95% B for 18 min. Mass spectrometry (MS) was performed on Q-Exactive Orbitrap mass spectrometer (Thermo Fisher Scientific) with the top 10 acquisition method: MS resolution 70,000, between 350 and 1,500 m/z, followed by MS/MS analysis (resolution 17,500) on the most intense 10 peaks. Raw MS data were processed using Proteome Discoverer (Thermo Fisher Scientific, version 2.2.0.388) with false-discovery rates < 0.01 at the levels of proteins and peptides. Enzyme specificity was set to trypsin, and the search included cysteine methylthiolation as a fixed modification, and N-acetylation of protein, oxidation of methionine, and phosphorylation of serine/threonine/tyrosine as variable modifications. Differential abundance significance was estimated from two biologically independent experiments (two technical replicates for each experiment) using background-based ANOVA with Benjamini-Hochberg correction to determine adjusted p-values.

For the pathway analysis, we selected proteins whose levels (log2-fold change) were oppositely affected by siRNA against *Inpp5d* and *Trem2* (*Inpp5d* vs *Trem2* > 1.5, *Inpp5d* vs non-target siRNA > 1, *Trem2* vs non-target siRNA < 1). Note that we included the proteins with sub-threshold p-values ($p > 0.05$) in the analysis. The gene-ontology term enrichment analysis was performed using DAVID (https://david.ncifcrf.gov/home.jsp) and the terms significant in the biological process (p-value < 0.05) were shown.

Adhesion assay of primary microglia

Forty-eight hours after siRNA transfection, primary microglia were trypsinized, allowed to attach to glass coverslips overnight, and primed with 1 μg/mL lipopolysaccharide (O111:B4, Sigma-Aldrich, Cat#L4391) for 3 h. The cells were fixed and labeled with Alexa Fluor 647-conjugated cholera toxin subunit B (Invitrogen) and DAPI. For quantification, randomly selected 10–11 fields for each of three biological replicates were photographed using EVOS microscope (Thermo Fisher Scientific). The total area occupied by cells was determined for each image and divided by the number of DAPI-positive nuclei to obtain mean cell area.

Chemotaxis assay of primary microglia

Forty-eight hours after siRNA transfection, primary microglia were replated onto a Transwell insert (8.0-μm pore, 24-well, Corning) at the density of 5.0×10^4 cells/well with 10% LCM. Twenty ng/mL recombinant murine complement component C5a (R&D Systems) was added to the bottom well to stimulate downward migration. After 24 h, the cells were fixed with freshly prepared 4% PFA at RT for 15 min, and stained with 0.5% Crystal violet in 25% methanol at RT for 15 min. The cells on the upper surface were removed with cotton swabs. Images of migrated cells were acquired using EVOS microscope. The mean number of migrated cells were determined from five fields for each insert per experiment.

alamarBlue assay of primary microglia

Cell viability was determined using the alamarBlue assay kit (Bio-Rad). Briefly, primary microglia were plated in a 96-well plate at a density of 1.5×10^4 cells/well with 10% LCM and transfected with siRNA on the next day. Seventy-two hours after transfection, the medium was replaced by those containing 10% alamarBlue. After 3 h of culturing, fluorescence was measured by spectrophotometer. Values were shown by normalizing to the value of non-transfected cells.

Co-immunoprecipitation experiment

HEK293A cells were transfected with plasmids encoding FLAG-tagged human *INPP5D*, HA-tagged human *TREM2* (an HA tag is inserted immediately after the signal sequence), and V5-tagged human *TYROBP*. Forty-eight hours after transfection, the cells were treated with or without 10 μM pervanadate for 30 min and then lysed with lysis buffer (50 mM Tris-HCl (pH 7.4), 150 mM NaCl, 1% Triton X-100, protease/phosphatase inhibitors). The lysates were precleared, incubated with anti-FLAG (FUJIFILM Wako, clone 1E6) or irrelevant mouse IgG at the concentration of 2 μg/mL overnight at 4°C, and then added with Protein G Sepharose 4 Fast Flow (Cytiva) for 2 h. After washing with lysis buffer, immunoprecipitates were eluted from the beads by boiling in SDS-PAGE sample buffer containing 2-mercaptoethanol.

In situ proximity ligation assay

The *in situ* PLA was performed on fixed primary microglia with Duolink *In Situ* PLA probes and Detection Reagents Green (Sigma-Aldrich) according to the manufacturer's instruction. Cells were permeabilized with 0.1% Triton X-100 in PBS for 5 min, incubated with blocking solution for 1 h at 37°C and then with pairs of primary antibodies (anti-TREM2 E7P8J, 1:250; anti-TYROBP D7G1X, 1:250; anti-INPP5D P1C1, 1:250; or anti-SYK SYK-01, 1:250) for 1 hr at RT. The cells were incubated with anti-mouse PLUS and anti-rabbit MINUS for 1 h at 37°C, followed by ligation reaction for 30 min and then by the rolling circle amplification for 100 min at 37°C. Finally, the cells were mounted with ProLong Diamond Antifade Mountant with DAPI. For quantification, randomly selected 9–13 fields for each of 2–4 biological replicates were photographed using EVOS microscope. The total number of PLA dots determined for each image was divided by the number of DAPI-positive nuclei to obtain mean number of dots per cell. The data were shown as relative to the averaged value of control group.

INPP5D overexpression in MG6 cells and antibody-mediated stimulation of TREM2

Immortalized mouse microglial cell line MG6[97,98] was maintained in 10% LCM. Doxycycline-inducible lentiviral expression vectors for FLAG-tagged full-length INPP5D (wild-type and phosphatase-dead mutant D672A) were constructed by replacing Cas9 cassette from pCW-Cas9 (a gift from Eric Lander & David Sabatini; Addgene plasmid #50661; http://n2t.net/addgene:50661; RRID:Addgene_50661). Cells infected with the recombinant lentivirus were selected with 4 μg/mL puromycin, plated at a density of 5.0×10^4 cells/48-well in medium containing 5 μg/mL doxycycline and cultured for 48 h. The cells were then starved with HBSS(+) for 30 min, followed by stimulation with 15 μg/mL anti-TREM2 antibody (AF1729) or normal sheep IgG in HBSS(+) for 5 min, and harvested for immunoblotting. The antibodies were used after purification with Amicon Ultra device to remove sodium azide.

RNA sequencing

Total RNA was extracted from at least more than 12,000 isolated microglia for each sample using RNeasy Plus Micro Kit (QIAGEN, Cat#74034) according to the manufacturer's instructions. RNA sequence library preparation, sequencing and mapping were performed by DNAFORM (Yokohama, Kanagawa, Japan). Qualities of RNA were assessed by Bioanalyzer (Agilent) to ensure that RNA integrity number is over 9.0. Double-stranded cDNA libraries were prepared using SMART-Seq v4 Ultra Low Input RNA Kit for Sequencing (TaKaRa) according to the manufacturer's instruction and were sequenced using paired end reads (150 bp) on HiSeq. Obtained reads were mapped onto the mouse GRCm38.p6 (mm10) genome using STAR (version 2.7.3a). Total and mapped counts of reads for each sample were summarized in Table S2. Reads on annotated genes were counted using featureCounts (version 1.6.4). The count data were analyzed using TCC-GUI[59] to identify DEGs.

qRT-PCR

Complementary DNA (cDNA) was prepared from extracted RNA using ReverTra Ace qPCR RT Master Mix with gDNA Remover (FSQ-301, TOYOBO) according to the manufacturer's instructions. cDNA was diluted in 1/25 with Milli-Q and used for the assay. Real-time reverse transcription was performed in duplicate using THUNDERBIRD SYBR qPCR Mix (QPS-201, TOYOBO) according to the manufacturer's instructions in a LightCycler 480 Instrument II (Roche). Standard curves were generated for each gene by diluting one of the samples in 1/5, 1/25 and 1/125 with Milli-Q. Changes in gene expression were measured by comparative analysis of qRT-PCR by CT method which was normalized to *Gapdh* expression. The primers used in the assay were listed in Table S1.

Image acquisition and analysis

Samples belonging to the same experiment were imaged during the same imaging session by using confocal laser scanning microscopy TCS-SP5 (Leica) or spinning disc microscopy Dragonfly 505 (Andor Technology). Super resolution images of Thioflavin S were acquired by LSM980 with Airyscan2 (Carl Zeiss Microscopy).

If there is no additional description, five z-slices at the interval of 10 μm were obtained at 10× magnification for IBA1 (coverage analysis) and GFAP, or 20× magnification for PU.1, dystrophic neurite markers, Cd11c and Tmem119. For most cases, tiled images were stitched to reconstitute an entire image of the coronal section, the entire or subregion (hippocampus, cortex) of which were used for analyses. Except for p-tau analysis, images were maximally projected to the x-y plane by using ImageJ or Imaris (Oxford Instruments). ImageJ was also used for other image processing and analyses. If needed, we applied "mean filter" or "median filter" function to reduce random noise and "subtract background" function to reduce overall image background. Following these pre-processing, respective automated image processes were performed to images by using custom ImageJ macros. The same ImageJ macro was applied to each image in the same experiment. The methods for image processing were summarized as below.

To quantify microglial coverage, the proportion of IBA1-positive area per individual Aβ plaque was calculated based on IBA1 and Aβ staining images that were preprocessed as follows. Aβ images were segmented by optimal threshold values determined by an automatic algorithm, and then by particle size. Considering that microglia approach Aβ plaques horizontally, the obtained binary images were dilated for 3 pixels to create Aβ plaque masks. IBA1 images were also segmented by optimal threshold values determined by an automatic algorithm to create IBA1 masks. Overlapping area between IBA1 and Aβ masks was normalized to plaque size as 100% for each plaque, and the average value of all plaques in each brain section was compared between groups. Otherwise, individual plaques in the hippocampal region were classified based on the IBA1-coverage into the following categories: dense (>40%), intermediate (20–40%) and sparse (<20%), and the proportion of each category was compared between groups.

To quantify the immunoreactive area for GFAP, BACE1, LAMP1, and ubiquitin, the following preprocessing and analyses were performed on selected subregions in the cortex (regions of interest; ROIs) instead of the entire section. The original images were segmented by optimal threshold values determined by an automatic algorithm. For the BACE1 and LAMP1 analyses, smaller particles were excluded as non-specific signals. For the ubiquitin analysis, ''watershed'' function was applied to the threshold images to distinguish neuritic plaques from non-specific staining of nuclei, and then smaller particles were excluded. Based on the obtained images, the immunoreactive area was calculated and normalized to the ROI area, and the value was compared between groups.

To quantify the number of microglia around Aβ plaques, PU.1-positive puncta were counted for each plaque based on PU.1 and Aβ staining images. Aβ masks were created as described above. PU.1 images were segmented by optimal threshold values determined by an automatic algorithm and were applied with the ''watershed'' function to distinguish adjacent PU.1-positive nuclei. The number of PU.1-positive puncta was determined for each plaque, and the average value of all plaques in each brain section was compared between groups.

To quantify colocalization of p-tau and Aβ plaques, p-tau immunoreactive area was determined for each plaque based on pre-processed p-tau and Aβ images. We found that satisfactory p-tau labeling was only achieved within several micrometers beneath the surface of brain sections, possibly due to poor tissue penetration of the peroxidase-conjugated antibody used in the TSA method. Therefore, instead of using projected images, we selected an optimal staining image at a certain z-position for the analysis. Aβ plaque masks were created as described above. P-tau images were segmented by optimal threshold values determined by an automatic algorithm. From the threshold images, smaller particles (corresponding to non-specific neuronal staining) were excluded to obtain plaque-associated p-tau masks. Overlapping area between the two masks was quantified and normalized to the plaque size as 100% for each Aβ plaque, and the average value of all plaques in each observed region was compared between groups.

To quantify the Thioflavin S staining of the plaques, images were segmented by optimal threshold values determined by an automatic algorithm. Smaller particles were excluded as non-specific signals. Mean intensities of individual plaques were determined, and the average value of all the plaques in each brain section was compared between groups.

QUANTIFICATION AND STATISTICAL ANALYSIS

Statistical analyses and graphical presentations were performed with GraphPad Prism 8/9 or the statistical language R. Data were analyzed by unpaired t-test with Welch's correction for two group comparisons. For multiple group comparisons, ordinary one-way ANOVA followed by Tukey's or Dunnett's multiple comparison test was used, except for Figures 7B, S6E, S6G, and S6N (using repeated measures one-way ANOVA followed by Tukey's test), Figure 1F (using two-way ANOVA followed by Tukey's test) and Figure S4B (using two-way ANOVA followed by Sidak's test). All error bars indicate the SE of mean. Sample sizes and any additional statistical details can be found in the figure legends. p-values lower than 0.05 were considered significant and represented by the following symbols: $^{*}p < 0.05$, $^{**}p < 0.01$, $^{***}p < 0.001$, $^{****}p < 0.0001$.